Petrological architecture of a magmatic shear zone: A multidisciplinary investigation of strain localisation during magma ascent at Unzen volcano, Japan

Paul A. Wallace[1*], Jackie E. Kendrick[1], Takahiro Miwa[2], James D. Ashworth[1], Rebecca Coats[1], James E.P. Utley[1], Sarah Henton De Angelis[1], Elisabetta Mariani[1], Andrew Biggin[1], Rhodri Kendrick[1], Setsuya Nakada[3], Takeshi Matsushima[4] and Yan Lavallée[1]

[1]Department of Earth, Ocean and Ecological Sciences, University of Liverpool, Liverpool L69 3GP, UK

[2] National Research Institute for Earth Science and Disaster Prevention, Ibaraki, 305-0006 Japan

[3]Earthquake Research Institute, University of Tokyo, Yayoi 1-1-1, Bunkyo, Tokyo, 113-0032 Japan

[4] Institute of Seismology and Volcanology, Faculty of Science, Kyushu University, Shin'yama 2-5643-29, Shimabara, Nagasaki, 855-0843 Japan

***Corresponding Author** Email: Paul.Wallace@liverpool.ac.uk (Paul Anthony Wallace)

Phone number: +44 (0) 151 794 5183

ABSTRACT

Shearing of magma during ascent can promote strain localisation near the conduit margins. Any mechanical and thermal discontinuities associated with such events may alter the chemical, physical and rheological stability of the magma, and thus its propensity to erupt. Lava spines can record such processes, preserving a range of macroscopic and microscopic deformation textures, attributed to shearing and friction, as magma ascends through the viscous-brittle transition. Here we use a multidisciplinary approach combining petrology, microstructures, crystallography, magnetics and experimentation to assess the evidence, role and extent of shearing across a marginal shear zone of the 1994–1995 lava spine at Unzen volcano, Japan. Our results show that crystals can effectively monitor stress conditions during magma ascent, with viscous remobilisation, crystal plasticity and comminution all systematically increasing towards the spine margin. Accompanying this, we find an increase in mineral destabilisation in the form of pargasitic amphibole breakdown displaying textural variations across the shear zone, from symplectitic to granular rims towards the spine margin. In addition, the compaction of pores, chemical and textural alteration of interstitial glass, and magnetic variations all change systematically with shear intensity. The strong correlation between the degree of shearing, crystal deformation and disequilibrium features, in addition to distinct magnetic properties, implies a localised thermal input due to shear and frictional processes near the conduit margin during magma ascent. This was accompanied by late-stage or post-emplacement fluid- and gas-induced alteration of the gouge, as well as oxidation and glass devitrification. Understanding and recognising evidence for strain localisation during magma ascent may therefore be vital when assessing factors that regulate the style of volcanic eruptions, which may provide insights into the cryptic shifts from effusive–explosive activity as observed at many active lava domes.

Keywords: Amphibole; Crystal plasticity; Lava spine; Shear heating; Strain localisation; Unzen volcano

INTRODUCTION

The characteristics of erupted lavas reflect a complex series of magmatic events from crystallisation, crystal segregation, chemical speciation, ascent, degassing, eruptive shearing and deposition. Strain localisation during the ascent of high viscosity magmas at lava domes may have an influential role on many pre-eruptive conduit processes as well as eruption dynamics. The ability for strain to preferentially localise during magma ascent is favoured by the magmas's non-Newtonian response, following crystallisation (e.g. Lejeune & Richet, 1995) and gas exsolution (e.g. Llewellin & Manga, 2004). This, in turn, can promote a transition from a Poiseuille to plug-like flow (Hale, 2007; Hale *et al.*, 2007), facilitating the formation of discrete shear zones near conduit margins (Hale & Wadge, 2008; Lavallée *et al.*, 2013) which may be more (Gaunt *et al.*, 2014) or less permeable (Kendrick *et al.*, 2013) than the bulk of the magma. Where marginal shear zones with relatively high permeabilities (Gaunt *et al.*, 2014) surround a relatively dense, degassed magma core, temporal sealing of these regions may cause gas pressure to accumulate below the plug and consequently fragment, causing explosive activity and/or dome destabilisation (Voight *et al.*, 1999; Mason *et al.*, 2006; Clarke *et al.*, 2007; Lensky *et al.*, 2008; Michaut *et al.*, 2009; Kennedy *et al.*, 2010; Ashwell *et al.*, 2015; Farquharson *et al.*, 2016; Heap *et al.*, 2017). Upon ascent, magma may encounter the viscous-brittle transition, beyond which, faulting processes can dominate (Kendrick *et al.*, 2012). If faulting extends to the surface, it may result in the extrusion of a lava spine piercing through the dome carapace, contributing to the exogenous growth of dome-building eruptions (Mount St. Helens, USA – e.g. Cashman *et al.*, 2008; Soufrière Hills volcano, Montserrat – e.g. Melnik & Sparks, 2002; Unzen volcano, Japan – e.g. Nakada *et al.*,

1999; and Mont Pelée, Martinique – e.g. Tanguy, 2004). Hence, a lava spine provides a relic of magma shearing and faulting processes in the shallow volcanic conduit.

Understanding the processes involved in spine extrusion may aid in constraining the complexities associated with ongoing eruptions at lava domes. Many lava domes are crystal-rich. Crystals have the propensity to physically interact within the flowing magma by partitioning strain (e.g. Caricchi *et al.*, 2007; Lavallée *et al.*, 2007; Picard *et al.*, 2011), promoting strain localisation (Cordonnier *et al.*, 2009; Lavallée *et al.*, 2012b; Lavallée *et al.*, 2013), and as such preserve deformation textures (e.g. Kendrick *et al.*, 2017). The interaction of crystals has been observed and parameterised in many experimental investigations (e.g. Caricchi *et al.*, 2007; Cordonnier *et al.*, 2009; Forien *et al.*, 2011; Picard *et al.*, 2011), being portrayed as acting to localise stress, forming a rigid network. However, stress concentration (e.g. Deubelbeiss *et al.*, 2011) may result in plastic deformation of the crystalline phase (Kendrick *et al.*, 2017) and even fracturing (Lavallée *et al.*, 2007; Cordonnier *et al.*, 2009; Forien *et al.*, 2011; Coats *et al.*, 2018) as magma undergoes the viscous-brittle transition. This characteristic suggests crystal-plasticity and fracturing of crystals (also termed comminution when induced by shear) may play roles in accommodating strain, and that crystals in erupted lavas can act as deformation markers of shallow volcanic processes. Until now, the extent of crystal plasticity has yet to be explored at outcrop scale, and its role remains unquantified.

Previous investigations on the mechanical processes of spine growth at Mount St. Helens observed multiple forms of evidence supporting brittle deformation at the conduit margin (e.g. Kennedy *et al.*, 2009), resulting in a 1–3 m thick mantle of gouge dominated by tensile fracturing, granulation and cataclasis, all thought to form at sub-solidus conditions at <1 km depth (Cashman *et al.*, 2008; Pallister *et al.*, 2013). The products revealed no microstructural evidence of subsequent annealing, high-temperature viscous flow or solid-state crystal plasticity (Cashman *et al.*, 2008; Kennedy *et al.*, 2009), although solid-state

sintering has been attributed to the lithification of fault gouge at the spine margin (Ryan *et al.*, 2018). However, Kendrick *et al.* (2012) examined the latest spine at Mount St. Helens, finding evidence for the role of rapid heating in the form of textural and microstructural evolution, complemented by geochemical, mineralogical, kinetic and magnetic analyses of the sheared region of the spine 7 margin.

It has become increasingly recognised, via theoretical models (e.g. Costa & Macedonio, 2003; Mastin, 2005; Vedeneeva *et al.*, 2005; Hale *et al.*, 2007), experimentation (e.g. Hess *et al.*, 2008; Lavallée *et al.*, 2012a; Kendrick *et al.*, 2014b; Hornby *et al.*, 2015) and detailed petrological constraints (e.g. Rosi *et al.*, 2004; Wright & Weinberg, 2009), that shear and/or frictional heating in areas of strain localisation may locally raise magmatic temperatures. Shear heating is a thermodynamic response to the dissipation of viscous energy (Ockendon, 2006); similarly, fault friction can also generate substantial thermal input (Carslaw & Jaeger, 1959). The plug-like flow that characterises the extrusion of lava domes makes them more susceptible to these thermal effects, contributing to shifts in rheology that dictate magma ascent dynamics. It has been proposed, based on numerical modelling, that temperature rises of >100 ºC near the conduit margins are attainable due to viscous deformation (Rosi *et al.*, 2004; Mastin, 2005; Costa *et al.*, 2007; Hale *et al.*, 2007). In contrast, fault friction, although localised on narrow planes, can generate a temperature rise of several hundred degrees (e.g. Lavallée *et al.*, 2012a; Kendrick *et al.*, 2014b; Hornby *et al.*, 2015; Lavallée *et al.*, 2015). Such temperature increases could alter the magma's physical and chemical properties; in detail, heating could: drive mineral reactions (e.g. De Angelis *et al.*, 2015), melt crystalline phases (e.g. Kendrick *et al.*, 2014b), re-set magnetic properties (e.g. Kendrick *et al.*, 2012), trigger vesiculation (Lavallée *et al.*, 2015), lower interstitial melt viscosity (e.g. Giordano *et al.*, 2008), redistribute and collapse pores (e.g. Laumonier *et al.*, 2011) altering degassing pathways (e.g. Kendrick *et al.*, 2014a; Ashwell *et al.*, 2015), and

more efficiently heal fractures (e.g. Tuffen *et al.*, 2003). In glass-bearing rocks at cooler temperatures, a thermal input could push them above the glass transition temperature (T_g), a kinetic barrier that is dependent on the timescales of structural relaxation where the glass softens to a melt (Dingwell & Webb, 1989; Webb & Dingwell, 1990), enabling viscous remobilisation (Hornby *et al.*, 2015; Lavallée *et al.*, 2015). Although becoming increasingly explored through laboratory experiments, few studies have documented the effects of shear or frictional heating in shallow volcanic conduits from a physical volcanology perspective (Smith *et al.*, 2001; Rosi *et al.*, 2004; Tuffen & Dingwell, 2005; Kendrick *et al.*, 2012; Kendrick *et al.*, 2014a; Hornby *et al.*, 2015; Lavallée *et al.*, 2015). Recognising evidence for strain localisation and the related thermal feedback processes should not be overlooked when assessing dome longevity and could contribute to relatively cryptic shifts in eruption style (Sparks, 1997; Cashman & Sparks, 2013; Cassidy *et al.*, 2018).

Spine extrusion during the closing of the 1991–1995 lava dome eruption and subsequent quiescence at Unzen volcano, Japan, provided a unique opportunity to explore the occurrence, extent and role of shearing on crystal deformation and thermal disequilibrium during magma ascent. Here, we present the first systematic study of the mineralogy, microstructures, crystal size and shape distribution, mineral stability, and magnetic properties across a sheared margin of the Unzen lava spine, in which we explore the results in the context of syn-emplacement deformation and subsequent alteration. The data are complemented by the first high-temperature, high-velocity rotary shear experiment on volcanic materials to simulate the conditions during eruptive shear.

Overview of the 1991–1995 dome eruption

Unzen volcano is a stratovolcano located in southwest Japan on the Shimabara Peninsula (Fig. 1a). Since its formation at ca. 500 ka, its historical activity has consisted dominantly of

thick lava flows, domes, and their subsequent collapse deposits, which range from andesite to dacite in composition, and notably lacks any extensive explosive episodes (Hoshizumi *et al.*, 1999; Nakada *et al.*, 1999). The latest eruption took place from 1991–1995 following 198 years of dormancy, leading to the growth of a dacitic lava dome (Fig. 1b) in which the eruptive products have a narrow range of compositional variability from 64.5–66.0 wt % SiO_2 (Nakada & Motomura, 1999). A full description of the 1991–1995 dome-building eruption has been given by Nakada *et al.* (1999) and is briefly summarised here. On 20 May 1991, a dacitic lava dome appeared for the first time on Unzen volcano after persistent phreatic and phreatomagmatic activity several months prior (Nakada & Motomura, 1999; Nakada *et al.*, 1999). The eruption lasted ~4 years and was the most voluminous in Unzen's history, being temporally characterised by two styles of dome growth; exogenous and endogenous. Exogenous growth occurred when effusion rates were high from May 1991–November 1993 (Nakada *et al.*, 1995; Nakada & Motomura, 1999), which contributed to the formation of 13 lava lobes (Sato *et al.*, 1992; Nakada & Fujii, 1993; Nakada & Motomura, 1999; Nakada *et al.*, 1999) and repetitive dome collapse events generating block-and-ash flows and pyroclastic density currents (Yamamoto *et al.*, 1993; Miyabuchi, 1999; Ui *et al.*, 1999; Sakuma *et al.*, 2008). The dome grew endogenously when effusion rates waned (from November 1993 onwards) causing rhythmic inflation-deflation cycles (Nakada & Motomura, 1999; Nakada *et al.*, 1999). By mid-October 1994–mid-February 1995 exogenic growth resumed as a lava spine extruded from the western limits of the endogenous crater (Fig. 1c and d; Nakada & Motomura, 1999; Nakada *et al.*, 1999; Saito & Shikawa, 2007). Spine growth was accompanied by tilt cycles and shallow swarms of seismicity in 40–60 hour cycles (Nakada *et al.*, 1999; Yamashina *et al.*, 1999; Umakoshi *et al.*, 2008), attributed to pressure fluctuations (Hendrasto *et al.*, 1997; Kohno *et al.*, 2008) or traction during fault-controlled pulsatory magma ascent (Hornby *et al.*, 2015; Lamb *et al.*, 2015). The spine extruded obliquely at an

angle of ~45º towards the east-south-east, consistent with the inclined nature of the conduit (Umakoshi *et al.*, 2001; Kohno *et al.*, 2008; Tanaka, 2016), with a final dimension of 150 m long, 30 m wide and 60 m high (Nakada *et al.*, 1999). After the eruption ended, cooling contraction of the underlying dome led to partial collapse of the spine leaving behind dissected blocks that were detached from the main spine (Fig. 1d; Nakada *et al.*, 1999).

Magma feeding the 1991–1995 eruption

Based on petrographic evidence from the erupted products, the eruption has been interpreted to be the result of magma mixing that took place within a ~7–8 km deep magma reservoir (e.g. Nakamura, 1995; Venezky & Rutherford, 1999; Holtz *et al.*, 2005; Kohno *et al.*, 2008; Sato *et al.*, 2017). The abundance of disequilibrium textures, including reverse zoned plagioclase and hornblende phenocrysts, diffusion profiles in magnetite phenocrysts and biotite reaction rims consisting of pargasitic amphibole and embayed quartz, has suggested interaction of two compositionally contrasting magmas (e.g. Nakada & Fujii, 1993; Nakamura, 1995; Nakada & Motomura, 1999; Venezky & Rutherford, 1999). These studies, along with experimental investigations, demonstrated that mixing involved a high-temperature (~1050 ºC) aphyric andesite and a low-temperature (~790 ºC) crystal-rich rhyodacite, resulting in a mixed 870–900 ºC dacite (Venezky & Rutherford, 1999; Holtz *et al.*, 2005). Most phenocrysts are interpreted to have been derived from the low-temperature end-member, whereas the groundmass assemblage is believed to be representative of a post-mixing mixed melt (Nakada & Motomura, 1999; Cichy *et al.*, 2011). The common occurrence of mafic enclaves further supports this model and has placed constraints on the contrasting residence times of the different magmas involved (Sato *et al.*, 2017). Fe-Ti oxide re-equilibration experiments have suggested that mixing took place a few weeks before the start of the eruption (Venezky & Rutherford, 1999), and that continuous or intermittent mixing

may have taken place throughout the eruptive period (e.g. Nakamura, 1995; Venezky & Rutherford, 1999; Holtz *et al.*, 2005). Although mixing likely continued during magma ascent from the magma reservoir (Nakada & Motomura, 1999), the Unzen Scientific Drilling Project demonstrated that the conduit from ca. 1 km depth consists of a thoroughly mixed dacite (Goto *et al.*, 2008).

METHODS

Sample collection

To explore evidence for strain localisation and its implications for the mineralogical signature of ascending magma, the focus of the study was directed to two intact shear zones (Fig. 2a and Fig. 3a). Outcrop 1 (Fig. 2a), located ~60 m east of the main spine (Latitude: 32.761313º Longitude: 130.299826º), represents a quasi-continuous gradation across a faulted margin of the spine. The shear zone is elongated towards the south-south-east (158º) with a dimension of 4.5 m long, 3.7 m wide and 2.5 m high. Based on the nature and degree of deformation observed, the shear zone was subdivided into four structurally discrete units (see Results section "Field observations" for description), including: gouge (Fig. 2b); a "high shear" zone (Fig. 2c, d and e) transitioning to a "moderate shear" zone (Fig. 2f and g); and a relatively undeformed core termed "low shear" (Fig. 2h and i) believed to be representative of the spine interior. Samples were collected along a transect of this shear zone (A–H in Fig. 2a), with all petrological and geochemical analysis in this study focusing exclusively on outcrop 1. For textural comparison, an undeformed dome block was collected from the talus (i.e. not from the spine), which represented material that was extruded immediately prior to spine growth and thus acts as a suitable baseline (Fig. 2j). Outcrop 2 (Fig. 3a) is the end-on exposure of a dissected portion of the east side of the main spine (Latitude: 32.761350° Longitude: 130.299444°), measuring >20 m wide by ~20 m high, and consisting of a relatively intact

interior, grading to a fractured and highly sheared zone with a sharp boundary to a narrow gouge layer bordered on the other side by a fault breccia (as described in Hornby *et al.*, 2015). This outcrop was used exclusively to assess magnetic variations across the faulted margin of the spine, along with loose blocks from the gouge, highly sheared and host (near-pristine spine interior) which were selected at outcrop 2 (Fig. 3b, c and d). All samples collected from outcrops 1 and 2 were thin sectioned perpendicular to the principle shear direction for petrographic analysis. Principle shear was characterised in each outcrop using *in situ* textural fabrics (e.g. lineations, elongated crystals, Riedel fractures) that reveal consistent orientations within the high shear zones with respect to the position of the gouge, with both outcrops displaying the upward shear motion of the extruded spine.

Geochemistry

Whole-rock geochemistry (across outcrop 1) was determined by X-ray Fluorescence (XRF) on a PANalytical Axios Advanced XRF spectrometer at the University of Leicester. Major elements were measured on glass beads fused from ignited powders using a sample to flux ratio of 1:5 (80% Li metaborate: 20% Li tetraborate). Results are reported as component oxide weight percent and have been recalculated to include loss on ignition (LOI). Trace elements were analysed using 32 mm diameter pressed powder pellets produced by mixing 7 g of fine ground sample powder with 12–15 drops of a 7 % polyvinyl alcohol solution (Moviol 8-88). Relative precisions and accuracies are better than 1–2 % for all major elements and better than 5 % for trace elements based on repeat analyses of international reference materials (BH-1 microgranodiorite, JR-1 rhyolite and BCR-1 basalt).

Electron microprobe (EPMA)

The major element composition of the interstitial glass (from outcrop 1) was determined using a Cameca SX-5 field-emission electron probe microanalyser (EPMA) at the University of Oxford. Element abundances were determined using wavelength dispersive spectroscopy (WDS) with TAP, PET and LIF crystals. Standards for calibration of the spectrometers included a range of silicates and oxides (e.g. albite for Na, Si, Al; wollastonite for Ca). Analyses were performed using a 15 kV accelerating voltage, 5 nA beam current and a defocused spot size of 5 μm. Due to a 5 μm spot size being used on glass, the concentrations of alkalis, namely Na and K, may show minor reduction; however, owing to the abundance of microlites and devitrified glass filaments, the use of a defocused 10 μm beam would have yielded higher inaccuracies. Major elements have a relative precision better than 3 % and an accuracy better than 5 %, except for Na which was better than 10%, based on repeat analyses of the KN-18 glass standard (comendite obsidian, Kenya). Our results are consistent with chemistry reported by Nakada & Motomura (1999) for partly devitrified glass and the results reveal relative chemical variations across the shear zone.

Automated SEM-EDS (QEMSCAN)

Mineral distribution and quantitative phase modality (of outcrop 1) was acquired using QEMSCAN (Quantitative Evaluation of Minerals by SCANning electron microscopy), an automated SEM-EDS system. It uses specially configured conventional SEM hardware and advanced highly adaptable software, manufactured by FEI. Each analysis was performed on an uncovered, polished and carbon coated thin section using a QEMSCAN WellSite at the University of Liverpool operating with a 15 kV accelerating voltage and ~5 nA beam current. Two Bruker energy dispersive X-ray spectrometers (EDS) recorded the discrete secondary X-rays emitted by the sample excited by the electron beam (within an interaction volume of ~10 μm^3), which are processed to identify and quantify the elements present and output a chemical

composition. The chemistry recorded is matched to known compositions for minerals, glasses and other chemically distinct phases. These phase compositions are stored in an extensive mineral database, referred to as a species identification protocol (SIP), which can be added to and edited by the user (see Gottlieb *et al.*, 2000). The system cannot measure any crystallographic features, thus cannot differentiate between amorphous, crystalline or any chemically identical polymorphs (e.g. quartz, cristobalite and tridymite). Data was collected in field-scan mode, collecting X-rays in an automated raster pattern at a specified step size (Gottlieb *et al.*, 2000; Pirrie *et al.*, 2004). For bulk mineralogy, whole thin section scans were performed with X-rays collected at 20 μm intervals; to assess groundmass mineralogy a 2 μm step size was used. The electron beam dwells at each point until sufficient X-rays are collected by the detectors to allow for successful phase matching (set to collect 1000 X-rays per point). A re-calibration of the system was performed after every sample exchange from the machine. Data processing and interpretation were performed using iDiscover software, which stitches the resulting data to form a continuous colour image of the sample, where each colour represents a different phase. Mineral statistics were obtained from the sum of the number of pixels of each phase and are normalised on a pore-free basis to provide a quantitative 2-D modal mineralogy (e.g. Pirrie *et al.*, 2004; Ayling *et al.*, 2012). The resolution (10 μm or 2 μm) does not influence the calculated mineralogy as there was no change in the beam operating conditions (i.e. interaction volume), only the spacing between analyses. Any phases smaller than the beams interaction volume will not be identified individually but incorporated with the chemistry of their surroundings (e.g. crystals less than ~2 μm in diameter surrounded by glass). Although 100 % reproducibility of a different thin section of the same material is unlikely (simple thin section effect), precision errors based on repeat scans after removing and reinserting the same thin section produced standard deviations <0.39 for all phases.

Image acquisition and analysis

Optical and scanning electron microscopy (SEM)

Optical microscopy enabled the identification and comparison of the major phases and any microstructural variations across the samples. Plane polarised light (PPL) images and whole thin section scans were acquired using a Leica DM2500P microscope, at a magnification of 2.5x, and a Leica DFC295 camera with a pixel resolution of 5 x 5 μm. SEM analysis was conducted using a Philips XL30 tungsten filament scanning electron microscope and Hitachi TM3000 at the University of Liverpool. Samples imaged using the Philips XL30 were carbon coated and imaged using a 20 kV beam, a working distance of 25 mm and a spot size of 5 μm, whereas the Hitachi TM3000 used a 15 kV beam and 10 mm working distance, both operating in backscattered electron (BSE) mode.

Plagioclase crystal size- and shape-distribution

Whole thin section microphotograph maps (from outcrop 1) collected in PPL were used to determine crystal size and shape variations of plagioclase phenocrysts across the shear zone to quantify crystal fracturing. The analysis was carried out using the National Institute of Health (NIH) ImageJ software package (Schneider *et al.*, 2012), where scans were converted to binary images, replacing all plagioclase crystals with black pixels and all other phases, including pores, with white pixels. To prevent misidentification of plagioclase with quartz in the binary conversion process, QEMSCAN maps were used as a guide to ensure all black pixels were correctly identified as plagioclase. Measurements were made on phenocrysts above a detection limit of 0.01 mm^2, ensuring all crystals above this size fraction were measured and shapes were accurately represented. Crystal size measurements included major and minor axis length (using the "fit ellipse" tool) and total area. Crystal shape was determined using the "shape descriptors" tool (circularity, aspect ratio, roundness and

solidity). Circularity of each phenocryst in the thin section was calculated using: **Circularity** = $\mathbf{4\pi(A/p^2)}$, where **A** is crystal area and **p** is the perimeter. Circularity values range from 0–1, with 1 indicating a perfect circle, becoming more elongate as values approach 0.

Groundmass pargasite reaction rims

High-magnification BSE images of pargasitic amphibole crystals in the groundmass were collected from each section of the outcrop 1 shear zone (gouge, high shear, moderate shear and low shear zones in Fig. 2a) and the undeformed dome rock (Fig. 2j). Reaction rim thickness variations were quantitatively assessed using ImageJ. The size of the pargasite crystals was determined using the longest axis, and when permitted, using the C-axis. Due to the irregular and patchy occurrence of breakdown rims within a single crystal, the thickest part of the rim was measured. Data were collected for >30 pargasite crystals from each zone, ensuring to cover the whole thin section to avoid misrepresentation.

Electron Backscatter Diffraction (EBSD)

Permanent internal deformation of a crystal lattice can provide useful insights into the stress conditions a material is exposed to during its history. Crystal plasticity is an isovolumetric deformation process derived from external forces exceeding the yield stress of a crystal lattice (Poirier, 1995), manifesting in a permanent strain by generating internal stranded dislocations. Dislocations cause a distortion of the crystal lattice structure and this distortion can be measured by electron backscatter diffraction (EBSD) in the SEM as a crystallographic "misorientation" angle (Prior *et al.*, 1999; Prior *et al.*, 2009). The angular resolution of the technique is ±0.5º (e.g. Mariani *et al.*, 2009). Crystal lattice orientation mapping for the identification and quantification of crystal plasticity was carried out across the outcrop 1 shear zone using a CamScan X500 CrystalProbe field-emission gun (FEG) SEM using the AZtec

EBSD acquisition software from Oxford Instruments HKL. Analyses were performed using a 20 kV accelerating voltage and 30 nA beam current. The electron beam source column is tilted at 70º relative to the sample surface normal. EBSD maps were collected on plagioclase and biotite phenocrysts and plagioclase microlites. The area coverage of phenocryst maps was dependent on the size of the target crystal, whereas microlites were analysed within a ~150 x 120 μm area from two or more locations within the same thin section to ensure accurate representation of each sample (see Supplementary Data Fig. S1 for the mapped areas). Acquisition of the data was performed using Oxford Instruments HKL AZtec EBSD software using step sizes from 0.15–0.4 μm for microlites and 2 μm for phenocrysts. Minerals were identified using energy dispersive point analyses (EDS) to determine their chemistry and mapped by EBSD using the appropriate crystallographic match units for each of the phases investigated. For statistical representation, >40 plagioclase microlites from each section of the shear zone were analysed. Minerals were indexed using all 12 bands, 70 reflectors, 120 Hough resolution, band edges and 4 x 4 binning. Data processing was carried out using CHANNEL 5 software by Oxford Instruments HKL. Individual crystals in the EBSD maps were subjected to a "texture component" analysis, where each pixel (each EBSD data point) is colour-coded according to the degree of misorientation of the crystal lattice relative to a selected reference pixel. All reference pixels were selected from one end of the crystal as this more accurately reflects the relative distortion across the crystal and depicts the maximum misorientation. Similarly, misorientations were measured as profiles along the length of a crystal to give a quantitative description of the deformation experienced. For each crystal, the length and width were recorded, as well as the "maximum misorientation" along the major axis from the misorientation profile. "Misorientation per micron" values were determined by dividing the maximum misorientation by the long axis length of the crystal. Through using

the mean misorientation per micron, we can model the amount of lattice distortion expected in a plagioclase microlite for a given crystal length from each section of the shear zone.

Thermal analysis

The kinetic and thermal properties of the Unzen lava spine were measured using differential scanning calorimetry (DSC), performed on a Netzsch simultaneous thermal analyser (STA) Jupiter 449 F1 at the University of Liverpool, using a single sapphire crystal for calibration of specific heat capacity (C_p). C_p as a function of temperature was calculated using DSC, which can provide a thermal history of the sample, in particular, a quantification of the glass transition temperature (T_g). Due to the high crystallinities of Unzen spine lavas and thus the low proportion of pristine glass to obtain a well-defined T_g measurement, spine material was lightly crushed into mm-sized fragments and groundmass dominated grains were selectively plucked to increase the glass:crystal ratio and provide a more reliable T_g value. Thirty eight mg of lightly crushed, phenocryst-free sample chips of low shear material from outcrop 1 (Fig. 2i) were placed in a lidded platinum crucible (with a single hole in the centre of the lid) and heated at 10 ºC min^{-1} to 1000 ºC with a continuous 20 mL min^{-1} argon flow. The onset of the T_g interval is defined by an exothermic deflection (increase) in the DSC and C_p curves.

Magnetic properties

Magmas that have undergone extensive shearing and faulting are ideal candidates to display magnetic anomalies due to alignments of the magnetic carriers (Hayman *et al.*, 2004) or a heating event associated with such processes (Nakamura *et al.*, 2002; Ferré *et al.*, 2005). The temperature dependent bulk magnetic susceptibility was measured on crushed chips (~140 g per measurement) from loose, *in situ* blocks from the outcrop 2 shear zone (undeformed host rock, Fig. 3b; highly sheared coherent lava, Fig. 3c; gouge, Fig. 3d). These were measured in

an Agico MFK1-FA Kappabridge with CS4/CS-L high/low-temperature attachments to measure the change in magnetic susceptibility across the temperature range of -200 to 700 ºC (using 4–5 repeats of each sample to verify the results). To complement the laboratory measurements a Bartington MS2 surface scanning probe to measure magnetic susceptibility was utilised on the lava dome to non-destructively measure the *in situ* distribution of susceptibility, with each measurement taken over a 20 cm circular area. Our measurements were performed across two transects of the spine margin shear zone (Fig. 3a) and on a selection of loose dome blocks that were categorised as either undeformed or deformed. A Magnetic Measurements Variable Field Translation Balance (MMVFTB) was further utilised to measure the Isothermal Remanent Magnetisation (IRM), backfield, hysteresis and thermomagnetic signal to identify magnetic grains and their domain states. Here, 4 or 5 measurements were made from crushed powder (~100 g per measurement) of the host, high shear and gouge material. The MMVFTB dataset was analysed using the RockMagAnalyzer software by Leonhardt (2006).

Experimental simulation

Experimental investigations on the co-existence of contrasting deformation textures in volcanic rocks (i.e. viscous, ductile and brittle) have primarily focused on the rheological implications associated with crystal interactions (e.g. Picard *et al.*, 2011). These experiments provide useful insights into magma behaviour under varying stress conditions in the volcanic conduit, which can influence bulk magma rheology. To explore the role of magma shearing within a volcanic conduit and assess a materials' textural response to such a process, we experimentally recreated conduit margin processes using a high-temperature high-velocity rotary shear (HVR) apparatus. The experiment was performed on a second-generation HVR at the University of Liverpool (see Hirose & Shimamoto, 2005 for details of the first-generation

HVR) using the natural, undeformed dome rock (as seen in Fig. 2j) as the starting material. The experiments involved the preparation of two 24.98 mm diameter plane parallel cylindrical cores with a 9 mm hollow centre, designed to create a ~8 mm wide annulus that would minimise any variations in slip rate across the contact surface. The two cores were placed inside the experimental apparatus, each connected to a separate piston so that during the experimental run one core would remain stationary and the other would rotate. Before placing the cores in direct contact, they were enclosed within a furnace and heated to 600 ºC at a rate of 20 ºC min^{-1}. This temperature was chosen for two reasons: 1) it represents a reasonable low-end temperature estimate of spine extrusion (with no recorded data available), which is also equivalent to temperatures estimated for the volcanic conduit at Mount St. Helens during faulting (Pallister *et al.*, 2013) and moreover, 2) it was below the solidus and T_g, thus any textural features observed could be directly related to shear and frictional heating and not the initial heating stage. After allowing ~30 minutes for thermal equilibration, a controlled axial load was applied and held constant using an air actuator on the non-rotating piston, corresponding to a normal stress of 2 MPa applied across the sample interface. The other piston and sample were rotated at 1150 rpm, equating to an equivalent slip rate of 1 ms^{-1} in direct shear (for sample geometry, see Shimamoto & Tsutsumi, 1994; Hirose & Shimamoto, 2005), analogous to conduit conditions previously estimated at Unzen volcano (Hornby *et al.*, 2015). The torque, axial load and sample shortening (using an externally-mounted strain-gauge with 10 mm scale) were measured for the duration of the experiment and used to calculate the continuous slip rate, normal stress and shear stress at 100 Hz. During the experimental run, the samples were recorded using a FLIR X6000sc infrared thermographic camera through a sapphire window of the furnace at a pixel resolution of 90 x 90 μm and 30 frames per second to monitor the temperature change due to frictional and shear heating along the simulated shear zone. It should be noted that these recorded

temperatures only depict that of the sample surface and may slightly underestimate the slip zones' internal temperature.

RESULTS

Field observations

Lava dome blocks

Lava blocks on the talus and summit of the Unzen lava dome are extremely heterogeneous (Fig. 1c). The characteristic differences of these blocks come most noticeably from their varying degrees of deformation, ranging from relatively undeformed (Fig. 1e and f) to complex deformation fabrics (i.e. sheared; Fig. 1g and h). All blocks display varying degrees of discolouration from pale grey to reddish-brown (Fig. 1c). Blocks that were classified as undeformed were distinguished by their massive nature (Fig. 1e), consisting of large, euhedral phenocrysts of plagioclase and amphibole, in addition to lacking any systematic textural anisotropy (Fig. 1f). Deformed or sheared blocks were characterised by the presence of at least one (but typically a combination) of the following: flow bands, systematic fractures (often conjugate), alignment of crystals or pores, and, in extreme cases, smeared plagioclase crystals visible to the naked eye (Fig. 1g and h). The porosity of these blocks is also quite variable, consistent with the porosity range of 8–33 % constrained for Unzen dome rocks (Kueppers *et al.*, 2005; Coats *et al.*, 2018), reiterating the heterogeneity of its deposits. The size of the blocks and proportion of sheared to undeformed material varies depending on the distance from the summit, which is observed succinctly on the western side of the dome (Fig. 1c). At the base of the talus, dome blocks are smaller (~1–2 m), more uniform in size and are typically less deformed. Further up the dome, blocks become larger (~2–4 m) with an increasing proportion of blocks hosting shear textures. The summit shows the most

heterogeneity, exposing multiple shear zones, cataclastic structures and sintered breccia either as fallen slabs surrounding the spine or larger *in situ* units (Fig. 1d).

Lava spine shear zones

Detailed structural surveys of the spine (Fig. 1d) in Autumn 2013 and Summer 2016 revealed an abundance of contemporaneous deformation fabrics at the margins, including evidence for the co-existence of dilatational and compactional shear zones. Outcrop 1 shear zone (Fig. 2a) can be separated into four discrete zones based on lateral variations in the style and intensity of deformation:

- Gouge: A <0.2 m thick, well-consolidated gouge layer is agglutinated onto the outcrops' western limit. The gouge is matrix-supported (i.e. a groundmass to crystal ratio of ~60:40) and dominated by cataclastic deformation (Fig. 2b), including conjugate fractures, trails of broken grains, clusters of angular crystal fragments (e.g. plagioclase and amphibole) and a poorly sorted reddish matrix consisting of ostensibly sintered finer material (<2 mm). Rounded dacitic clasts up to 15 mm in diameter are incorporated into the gouge, distinguished by their pale-yellow groundmass and structural integrity (Fig 2b).
- High shear zone: Directly adjoining the gouge, the high shear zone takes the form of a narrow (0.1–0.2 m wide) region comprised of undulating white-yellow porphyritic filaments/lenses surrounded by a reddish-brown groundmass that runs parallel to the gouge contact (Fig. 2c and d). Optically, these filaments appear to be partially filled with remnant fragments of broken crystals, commonly plagioclase, with any excavated fragments leaving behind elongated voids. These filaments were traceable on two sides of the outcrop (A–C and C–H in Fig. 2a), which revealed a planar orientation of NEE-SWW and provided a principle shear direction of NNW-SSE. These elongated

filaments grade into a 0.5 m wide zone displaying principle and Riedel shear lineations on the outcrops' external surface (between sample D and E in Fig. 2a), indicative of the upwards sinistral motion of the spine. In this section of the high shear zone, crystal filaments become less clear and individual crystals are more visible (Fig. 2e). However, all crystals within the high shear zone take the form of broken, angular fragments that rarely exceed 1 mm and are often aligned in the extrusion direction (optical images in Fig. 2c, d and e), with no crystals remaining intact.

- Moderate shear zone: A ~2 m thick zone which displays a reduction in principle shear intensity and lacks secondary Riedel features (E and F in Fig. 2a). Cataclastic structures are less intense, although still a predominant appearance. Crystals are significantly more visible, representing larger fragments compared to those observed in the high shear zone (up to 2 mm), although they still display alignment in the extrusion direction. Rare elongated mafic enclaves (top left of Fig. 2f) are also observed, which were not visible at outcrop scale in the high shear zone likely owing to their extreme flattening and the overprint of principle shear lineations.
- Low shear zone: The moderate shear zone grades into a >1.5 m thick section consisting of negligible deformation. It has a smooth, reddish external surface and displays large (up to 5 mm), euhedral phenocrysts of plagioclase, amphibole and biotite, with little sign of fractured or aligned crystals. Mafic enclaves (up to 40 mm) are also observed (Fig. 2h), being texturally similar to those in the moderate shear zone, but more rounded. This zone is comparable to the undeformed, non-spine dome rock, both at outcrop and thin section scale (Fig. 2j).

Outcrop 2 (Fig. 3a), previously described by Smith *et al.* (2001) and Hornby *et al.* (2015), has been divided into three separate units. A <0.6 m wide red gouge layer (Fig. 3d) is mantled by a poorly-sorted, >6m thick massive fault breccia (right in Fig. 3a). Lenses of highly sheared

coherent lava are embedded into the gouge and elongated parallel to the gouge-breccia contact. A ~2 m wide high shear zone (Fig. 3a and c), texturally similar to that of outcrop 1 (Fig. 2c and d), lies to the left of the gouge, consisting of 20–40 mm elongated white filaments within a reddish-grey groundmass. Adjacent to this highly sheared region, a >8 m thick, relatively undeformed unit represents the core of the lava spine (termed host in Fig. 3a). Although the dacite here consists of large euhedral phenocrysts (up to 5 mm; Fig. 3b), with textures similar to those observed in the low shear zone of outcrop 1 (Fig. 2i), occasional high-porosity shear bands that extend up to 2 m in length run sub-parallel to the spine margin (see Smith *et al.*, 2001).

Bulk chemical heterogeneities

Bulk-rock chemistry of the lava spine reveals a dacitic composition (65.4–65.9 wt % SiO_2) with only subtle variations across the shear zone that are close to the analytical limit. Yet, it may be possible to distinguish each zone in Fig. 2a (gouge, high, moderate and low shear) from individual major and trace elements (Table 1). For major components, the gouge has the lowest concentration of SiO_2 and Na_2O, and highest Fe_2O_3 and MgO contents; directly in contact, the high shear zone has the highest SiO_2 and K_2O. The low shear zone has the highest CaO and Na_2O, together with the lowest Fe_2O_3, MgO and K_2O. The moderate shear zone falls compositionally intermediate between these zones. Trace elements may reflect further variations between each zone. For example, the gouge reveals the highest levels of Rb and Zr, with the low shear zone having the least. The high shear zone can be distinguished by the lowest Sr content and highest La and Ce, while the low shear zone can be identified by the highest Sr.

Mineralogy and petrography

The dacitic spine is porphyritic, consisting of phenocrysts and microphenocrysts (27–29 area %) of plagioclase (17–21 area %), amphibole (3.5–6.0 area %), biotite (2 area %) and quartz (1.5–3.5 area %). The groundmass contains 50–60 area % microlites of plagioclase, pargasitic amphibole, polymorphs of silica, pyroxene, Fe-Ti oxides and minor accessory minerals, set in a partially devitrified, peraluminous rhyolitic interstitial glass (ca. 79 wt % SiO_2). Plagioclase dominates the mineral assemblage, occurring as phenocrysts up to 5 mm long, tabular and equant microlites in the groundmass, mineral inclusions within hornblende phenocrysts, and as a breakdown product of hydrous mineral phases (i.e. amphibole and biotite). Two types of amphibole are found in the dacite; hornblende as phenocrysts and pargasite as microphenocrysts and microlites in the groundmass. The hornblendes occasionally display reaction rims, often patchy, consisting of pyroxene, plagioclase and Fe-Ti oxide microlites. Pargasite forms ellipsoidal crystals with occasional hollow cores and/or concentric zoning. Pargasites located in the spine shear zone display breakdown rims, which have not been reported in any other Unzen lava products from the eruption (e.g. Sato *et al.*, 1999). Biotite takes the form of large, tabular phenocrysts, often with distinct coarse-grained reaction rims of pargasite, plagioclase and pyroxene. Reaction rims on both hornblende and biotite phenocrysts are not exclusive to the spine and were also observed in pyroclastic flow deposits throughout the eruption (Nakada & Motomura, 1999), thus are not attributed to spine processes. Quartz often appears as resorbed fragmented phenocrysts (up to 2 mm) embedded within the groundmass (e.g. bottom left of photomicrograph in Fig. 2f). Fe-Ti oxides (magnetite and ilmenite) appear as rare microphenocrysts and small acicular microlites in the groundmass. Orthopyroxene and clinopyroxene are found either as groundmass microlites or within breakdown rims of biotite and amphibole. All samples reveal silica-rich patches in the groundmass, either filling voids or as a by-product of glass devitrification.

Variations in mineral abundance across the shear zone were assessed by QEMSCAN analysis. The resulting data are expressed as colour-coded maps, providing a visual distribution of chemically discrete phases (Fig. 4 and Fig. 5) and through isolating each phase a quantitative comparison can be made across the shear zone (Table 2). All samples consist of the same mineral assemblage, although subtle differences in both bulk (phenocrysts plus groundmass phases, Fig. 4) and groundmass phases (Fig. 5) are observed. Bulk plagioclase content is highest in the low shear zone (40.2 area %), with a systematic decrease in the moderate and high shear zone (37.2 and 34.4 area %, respectively), increasing slightly in the gouge (37.7 area %). Amphibole displays a similar pattern, although to a lesser extent, owing to its lower abundance. Bulk biotite and pure silica-phases show an opposite trend, both being lowest in the low shear zone and highest in the gouge. Total bulk glass content shows a subtle increase from the low shear zone to high shear zone (32.0–36.3 area %), with the gouge having significantly less glass than anywhere else in the outcrop (24.6 area %). However, it is important to note that these observed bulk mineralogical variations should be taken with some caution, owing to the natural heterogeneity of Unzen lava, plus the possible effect of highly fractured minerals being removed during sampling or thin section preparation of highly deformed material. This is observed by comparing field textures and photomicrographs of the high shear zone (Fig. 2c and d), which show the potential loss of plagioclase evacuating elongated voids.

Within the groundmass (Fig. 5), similar quantities of plagioclase microlites are observed in both the low and high shear zones (27.3 and 28.5 area %, respectively). Plagioclase abundance in the gouge groundmass is higher relative to the other zones (33.1 area %), which also corresponds to the presence of angular plagioclase fragments as remnants of phenocryst comminution. Groundmass amphibole (pargasite) also has minimal variation between the low and high shear zones (3.9 and 3.2 area %, respectively), although the gouge

displays a subtle increase (4.9 area %). Pyroxene microlites have a similar abundance across the shear zone (all <2 area % for combined ortho- and clinopyroxene). The most significant difference is observed within the Si polymorphs (Fig. 5). The low and high shear zones have a similar textural arrangement of large, isolated silica-patches (up to 50 μm) with a minor variation in abundance between them (17.0 and 14.8 area %, respectively). In the gouge, these larger silica-patches are absent, with the groundmass being dominated by small (<10 μm), more abundant (21.4 area %), silica-rich phases that are interconnected with the interstitial glass. These micron-sized silica-patches in the gouge correspond to its lower interstitial glass content (Table 2).

The porous network of the shear zone shows significant heterogeneities (Figs 4, 5 and Table 2). The 2D bulk porosity, visualised and quantified for each section of the shear zone by QEMSCAN (white in Fig. 4), is highest in the low shear zone (22.4 area %), slightly reduced in the moderate shear zone (19.0 area %) and lowest in the high shear zone (13.2 area %). Interestingly, the porosity of the gouge (16.1 area %) is higher than the high shear zone but less porous than the low shear zone. The pores in the moderate and high shear zones are found as elongated voids, typically localised around fractured plagioclase phenocrysts, and less commonly amphiboles; this coincides with the relative decrease in plagioclase and amphibole in these zones (Fig. 4 and Table 2). By incorporating these porosity values with the bulk mineralogy abundances (i.e. combined and normalised to 100 area %), the decrease in plagioclase and amphibole abundance from the low shear to high shear zone is significantly lower. Groundmass porosity also shows a similar reduction from the low shear to high shear zone (Fig. 5 and Table 2). In the low shear zone, pores are >10 μm in diameter and are commonly connected to form a permeable porous network, equating to a porosity of 18.7 area %. Pores in the high shear zone groundmass are significantly lower in both abundance (13.0 area %) and size (mostly <10 μm diameter), with the majority of pores being unconnected.

The gouge groundmass porosity is slightly higher than that in the low shear zone (19.2 area %), being derived from a combination of small (<5 μm diameter) isolated pores and occasional microfractures located between broken plagioclase fragments (Fig. 5).

Crystal deformation

Banding, alignment and crystal failure

Crystal deformation is a dominant feature of the spine due to crystals' ability to record textures during transport and bulk viscous flow of the magma. Crystal alignment in the high shear zone is a characteristic feature seen most notably by the preferential orientation of plagioclase microphenocrysts and microlites with their major axis aligned parallel to the extrusion direction, in addition to larger crystals displaying pressure shadows (labelled PS in Fig. 6a). These aligned microlites appear to be localised within flow bands that envelope larger phenocryst fragments. In the moderate shear zone (Fig. 6b), crystal alignment is still present, although subtle, with no evidence of banding or pressure shadows, whereas the low shear zone comprises freely suspended and randomly oriented crystals (Fig. 6c).

In order to investigate crystal deformation due to shearing, we focus on plagioclase owing to its high abundance and previously reported high sensitivity to stress (e.g. Cordonnier *et al.*, 2009; Picard *et al.*, 2011). The change in size and shape of plagioclase phenocrysts were investigated using thin section scans and binary maps (Fig. 7a; see Supplementary Data Electronic Appendix 1 for full quantitative data). Results show a reduction in crystal size with increasing shear (Fig. 7b), which can be qualitatively seen in the binary phase maps (Fig. 7a), with the low shear zone hosting larger, more euhedral crystals which systemically become more fractured towards the shear zone margin. Average plagioclase circularity measurements of samples from the low and moderate shear zone oscillate between 0.48–0.58. Circularity values for plagioclase crystals in sample C and D of the high shear zone (Fig. 7c) show a

slight decrease in circularity compared to crystals within the moderate shear zone (sample E in Fig. 7c), although still fall within the range recorded in the low shear zone. Where the high shear zone is directly adjacent to the gouge (sample B in Fig. 7c) plagioclase crystals have the lowest circularity values (mean 0.44), with the gouge displaying an abrupt increase (mean 0.56), which corresponds to the sharp boundary as observed at outcrop scale (Fig. 2a). Qualitatively, amphibole (the second most abundant phenocryst phase) reveals a similar reduction in size across the shear zone (Fig. 4 and 7a).

Biotite and plagioclase lattice distortion

EBSD was performed on both phenocryst and microlite phases across the shear zone. Crystal plasticity is the distortion of a crystal's lattice owing to its rotation brought about by the movement and accumulation of dislocations, which is quantified as a misorientation (Brewer *et al.*, 2006); the higher the misorientation value, the more distorted the crystal lattice. The variation in misorientation within a single crystal can be seen using colour-coded, texture component maps with the colours representing the relative distortion, or misorientation, of the crystal lattice with respect to a selected reference pixel. Misorientation maps on broken segments of a once intact plagioclase phenocryst from the gouge (segments 1–3 in Fig. 8a) reveal negligible plastic deformation, with all segments rarely exceeding a 1° misorientation, despite being fragmental. However, analysis of biotite phenocrysts reveals an overwhelming abundance of plastic deformation. This is a common feature in the high shear zone and gouge, where up to 60° of relative lattice distortion is observed (Fig. 8b). In some cases, biotite crystals have exceeded their plastic limit, causing the crystal to fracture in the areas of most lattice distortion (Fig. 8b). In the high shear zone, biotite plasticity is preceded by brittle failure along shear bands, with plasticity remaining in the intact segments (Fig. 8c). Biotite

plasticity is less common in the moderate shear zone, and not observed in the low shear zone or core of the spine.

In contrast to plagioclase phenocrysts, plastic deformation of plagioclase microlites within the spine shear zone is evident (Fig. 9a). The advantage of studying microlites is that they provide a statistically robust dataset, and any potential data bias due to internal heterogeneities within a single thin section can be removed by analysing multiple areas within the same sample. Accurately quantifying the degree of lattice distortion in plagioclase microlites involved manually drawing misorientation transects from one end of each crystal to the other (T1 and T2 in Fig. 9a). Through compiling the maximum misorientation angles from microlites within each section of the shear zone (Supplementary Data Electronic Appendix 2), lateral differences were identified. The unimodal distributions of lattice misorientations (Fig. 9b) show a shift towards higher angles from low to high shear zone and gouge. The low and moderate shear zones show that most microlites have <2º misorientation. The high shear zone and gouge reveal a broader microlite misorientation distribution with lattice distortions of >9º. Through calculating the misorientation per micron for each microlite (after Kendrick *et al.*, 2017) we can remove any bias that would be caused by comparing microlites of different lengths (Fig. 9c). We find that the mean and maximum misorientation per micron increases systematically from the low to high shear zone, with the gouge being slightly lower than the high shear zone. Using the mean misorientation per micron for each section of the shear zone (squares in Fig. 9c) and multiplying these by an infinite crystal length, we can provide a modelled estimation for the degree of lattice distortion for a given crystal length (line gradients in Fig. 9d). These modelled misorientation estimates reveal that microlites of the same length from each section of the shear zone, are more likely to display a higher degree of plasticity in the gouge and higher shear zone (Fig. 9d). EBSD analysis on the undeformed,

non-spine dome rock (Fig. 2j) shows that here microlites exhibit the lowest misorientation values (Fig. 9d) and are comparable to those located in the low shear zone of the spine.

Magnetic signatures

A portable magnetic susceptibility meter was utilised on the lava dome to non-destructively measure the *in situ* distribution of susceptibility across two transects of the spine margin shear zone at outcrop 2 (Figs 3a, 10a and 10b) and to measure a selection of loose dome blocks. The field measurements showed magnetic susceptibility values between 0.27–7.21 $x10^{-4}$ (SI) from more than 200 measurements, with the highest values seen in the undeformed spine host material and lowest values in the high shear zone and gouge (Fig. 10a and b). Field magnetic susceptibility measurements on loose blocks on the dome, categorised as undeformed and deformed, showed values in close agreement (Fig. 10c; mean 3.14 and 5.85 $x10^{-4}$ SI [range 1.29–6.53 and 3.04–10.05], respectively). Moreover, magnetic susceptibility measured in the laboratory using a Magnetic Measurements Ltd Variable Field Translation Balance (VFTB) on samples from the undeformed host rock, high shear zone, and gouge (Fig. 3b–d), also match closely (Fig. 10c; Table 3). The bulk susceptibility, measured using an Agico MFK1-FA Kappabridge, also showed a similar relationship, where the undeformed host has the highest susceptibility, with the high shear zone having a slightly lower bulk susceptibility and gouge the lowest. The temperature-dependence of the bulk susceptibility was also distinct between each zone (Fig. 10d). The host rock produced sharply dropping reversible curves indicative of a single, low coercivity phase of low-Ti titanomagnetite; in contrast, the high shear and, especially, the gouge rock produced less reversible curves with shallower, less abrupt drops at high-temperature that suggest an alteration of the magnetic carrier (Fig. 10d).

The VFTB data were analysed using the RockMagAnalyzer software (Leonhardt, 2006), from which Curie temperatures (T_C; Table 3) were identified from the thermomagnetic

curves (see Supplementary Data Fig. S2 for curves) using the method of Moskowitz (1981). For each sample set, only one Curie temperature was identified, and these correspond well to the terminal decrease of bulk susceptibility (Fig. 10d), being 521 ºC in the undeformed host, 507 ºC in the highly sheared rock and 544 ºC in the gouge.

Isothermal Remanent Magnetisation (IRM) and backfield curves show each zone almost fully saturates at 200 to 300 mT (see Supplementary Data Figs S3 and S4 for raw data). Quantitatively, the S300 parameter, a measure of the degree of saturation at 300 mT (Bloemendal *et al.*, 1992), records subtle differences between the host, high shear and gouge zones (0.99, 0.96 and 0.92, respectively; Table 3), but with all values close to 1. The dominant magnetic phase is low coercivity titanomagnetite. Coercivity of remanence values (B_{cr}; Table 3) are lowest in the undeformed material (35 mT), slightly higher in the highly sheared material (37 mT) and significantly higher in the gouge (53 mT). Higher associated ratios of saturation remanence to saturation magnetisation (M_{rs}/M_s) and coercive force (B_c; Figure 10e), in addition to a contrasting morphology of the hysteresis curves (see Supplementary Data Fig. S5), also highlights a distinct difference between the gouge and other zones of the spine; in particular, B_c values for host material consistently plot between the high shear zone and gouge. Further differences are recorded by calculating the shape parameter (σ_{hys}) from the hysteresis curve, which shows that all samples are "potbellied" to differing degrees. Plotting σ_{hys} against the coercivity ratio (B_{rh}/B_{cr}) highlights a systematic change from the host, high shear zone and gouge material (Fig. 10f, after Fabian, 2003). Henkel plots (Henkel, 1964) supplement this information, incorporating backfield and IRM data (i.e. remanence data) to identify the presence of a demagnetising field arising either from multi-domain (MD) effects or magnetostatic interactions between single-domain grains (see Supplementary Data Fig. S6 for raw data). Samples are plotted against ideal Stoner-Wohlfarth particles, or uniaxial non-interacting single-domain particles (Wohlfarth, 1958), and although

the gouge plots closest to this line, all data plot below the line, and as such all remanence carriers from each section of the shear zone deviate from this ideal behaviour. Hysteresis and backfield data can be combined into a Day plot (Day *et al.*, 1977) to examine the domain state of the magnetic carriers. All sample sets are repeatable, and plot in distinctly different areas (Fig. 10g). Although all points fall within the pseudo-single-domain (PSD) region for pure magnetite (Dunlop, 2002), the Day plot again indicates the tendency for gouge to be considerably more single-domain-like, with the host rock again falling between the highly sheared zone and the gouge.

Groundmass textures and glass chemistry

Amphibole reaction rims

The two populations of amphibole that are present in the dacitic spine are hornblende phenocrysts and pargasite microphenocrysts and microlites in the groundmass. Reaction rims have previously been identified on hornblende phenocrysts within the pyroclastic deposits of the 1991–1995 eruption (e.g. Nakada & Motomura, 1999), with no reports of rims on groundmass pargasite. Within the spine shear zone, reaction rims on hornblende phenocrysts are similar in appearance to those reported in the pyroclastic deposits, thus are not discussed further.

Groundmass pargasite breakdown rims vary from those seen in hornblende phenocrysts, showing two types of breakdown texture: symplectitic and granular (Fig. 11a; see Supplementary Data Fig. S7 for additional examples). In the low and moderate shear zone, symplectitic rims mantle pargasite, termed based on the submicron interconnection of pyroxene, plagioclase and Fe-Ti oxide laths. In the high shear zone, these symplectitic rims are occasionally surrounded by coarser, detached pyroxene microlites (Fig. 11a). Pargasite in the gouge consists exclusively of a detached granular rim of pyroxene and Fe-Ti oxide

microlites. Minor symplectitic patches are occasionally seen on the inner zone of these detached granular rims, directly in contact with the host pargasite. Within the undeformed dome rock, only minor symplectitic patches are observed, with some pargasite crystals showing no evidence of reaction. To quantify this variation, the maximum thickness of each rim was measured from each section of the shear zone (Fig. 11b; Supplementary Data Electronic Appendix 3). Reaction rims are thickest in the gouge and high shear zone (maximum of 13.8 and 12.7 μm, respectively), and thinnest in the low shear zone and undeformed dome rock (maximum 4.8 μm and 3.2 μm, respectively), with the latter, occasionally displaying no rims. These changes are systematic across the shear zone and undeformed dome rock from: (1) unreacted pargasite as observed in undeformed dome material; (2) thin symplectitic rims in the low and moderate shear zone; (3) thicker symplectitic rims and the first appearance of granular rims in the high shear zone; (4) pronounced detached granular rims in the gouge.

Textural, chemical and thermal properties of the interstitial glass

The solid groundmass of the dacitic lava spine's shear zone consists of 33.5–47.8 area % interstitial glass (Table 2). Heterogeneous glass alteration textures are a prominent feature associated with the spine (Fig. 11a). In the low shear zone, clusters of fine-grained (<1–2 μm diameter), dark grey, silica-rich phases are observed within the glass, notably localised around plagioclase microlite edges. The moderate shear zone also consists of these silica-rich phases, which appear to be interconnected with web-like intergrowths that radiate in a spherulitic manner. These silica phases and intergrowths are most extensively seen within the high shear zone, where less pristine glass remains relative to the low shear zone. Despite these somewhat systematic differences between the low, moderate and high shear zone, the groundmass of the gouge is texturally different (Fig. 11a). The gouge consists of larger (5–10 μm in diameter),

subhedral silica phases, often displaying a scaly texture that forms an intercrystalline network around plagioclase microlites, with no web-like intergrowths and only minor interstitial glass remaining (as also recorded by QEMSCAN in Fig. 5 and Table 2). EBSD band contrast maps of the gouge (Fig. 9a and Supplementary Data Fig. S1), which only detect phases with a definite crystalline structure (i.e. will not detect glass or any other amorphous phases), identify these silica phases as crystalline, likely cristobalite.

The groundmass glass is rhyolitic (77–81 SiO_2 wt %), with subtle chemical variations between each section of the shear zone (Fig. 12; Table 4). Interstitial glass of the low and moderate shear zone has similar overlapping compositions for most major elements, particularly in SiO_2 (Fig. 12a; 79.9–81.3 and 79.8–81.4 wt %, respectively), although some elements in the moderate shear zone display a larger range (e.g. Al_2O_3 and Na_2O; Fig. 12b and c). The high shear zone consists of the most chemically heterogeneous glass; SiO_2 extends ~2 wt % below that recorded for the moderate and low shear zone (78.1–80.9 wt %). Opposingly, most other elements extend towards higher values, most notably for Al_2O_3 and Na_2O (Fig. 12b and c), with low concentration elements (e.g. MgO and CaO) falling within the range observed in the moderate and low shear zones. The interstitial glass of the gouge has the least SiO_2 (Fig. 12a; 77.1–79.1 wt %), but highest Al_2O_3, K_2O and Na_2O (Fig. 12b and c) with respect to the other zones. MgO (Fig. 12d) is lower in the gouge relative to the high shear zone, although it is within range of the moderate and low shear zones. These seemingly systematic chemical changes in the interstitial glass across the shear zone, decreasing in SiO_2 from the low and moderate shear zone towards the gouge, and an overall shift towards higher concentrations for other elements, is concordant with the increased appearance of crystalline silica in the groundmass. A simple mass balance using the average glass composition of the low shear zone (Table 4) reveals ~6 and ~14 % crystallisation of an SiO_2 polymorph (assuming 100 wt % SiO_2) is required to change the chemistry to that measured in the high

shear zone and gouge, respectively. This is consistent with both the groundmass textures (Fig. 11a) and reduction of glass content in the gouge (Fig 5 and Table 2). Although no reduction of glass was recorded for the high shear zone, this may be related to the <2 μm silica phases in this region being smaller than the beam's interaction volume (~10 μm^3) thus being classified as glass in QEMSCAN analysis.

Thermal analysis of the low shear zone groundmass material was performed to collate a thermal history of the magma, and, in particular, an estimation of the temperature at which viscous deformation may ensue, as determined by the glass transition (T_g). For the analysis, low shear zone material was used as it was considered the most representative of the magma's groundmass prior to deformation and any chemical alteration. A calorimetric T_g value of 790 ºC was obtained (using the C_p curve in Supplementary Data Fig. S8 based on a 10 $ºC.min^{-1}$ heating/cooling rate). This value was consistent with the estimated temperature derived from the viscosity model of Giordano *et al.* (2008) using measured glass chemistry (773 ºC) which acts as a viscosity gauge for 10^{12} Pa.s.

Experimental insights

At the imposed experimental conditions (2 MPa normal stress and 1 m s^{-1} slip rate), frictional work resulted in a rapid temperature rise of the dacite from 600 ºC to >1150 ºC in ~2 seconds (Fig. 13a, b and see Supplementary Data Fig. S9 for raw mechanical data), permitting localised melting of the rock along a narrow slip plane. After ~5 seconds of slip, a full melt layer had formed causing the heat source to transition from frictional heat to viscous dissipation (i.e. shear heating; e.g. Hirose & Shimamoto, 2005), as recorded by the appearance of shear bands radiating from the slip zone (Fig. 13b). Temperature profiles across the simulated shear zone (Fig. 13a) reveal a gradual increase in width through time as the temperature exceeds the calorimetric T_g. Microtextural observations of the material adjacent

to the melt zone show microlites and microphenocrysts are preferentially aligned in the direction of slip (Fig. 13c and d). Within this localised region, pores are reduced in both size and abundance, from ~40–100 μm in diameter in the starting material to <10 μm in diameter in the areas directly adjacent to the slip zone (Fig. 13e). A closer examination of the textures in the experimental shear zone (Fig. 13f) reveals localised reaction rims on pargasite microlites adjacent to the melt zone. Rims closest to the melt zone consist of coarse grained, detached pyroxene microlites (Fig. 13g), which become finer grained and more acicular further away (Fig. 13h). Pargasites away from the experimental shear zone (i.e. in the starting material) show negligible reaction rims and appear stable in the absence of shearing (Fig. 13i). Textural characteristics of the reaction rims in the experimental shear zone are similar to those in the natural gouge and high shear zone of the spine (Fig. 13j), while pargasite crystals in the low shear zone are more comparable to the starting material (Fig. 11a). Based on the microtextural differences induced across the experimental shear zone, it can be subdivided into discrete zones akin to the outcrop 1 shear zone (Fig. 2a and Fig. 13f): (1) a "low shear zone" with randomly oriented microlites, large open pores and no reaction rims on pargasite microlites; (2) a "moderate shear zone" with the onset of a reduction in porosity and thin reaction rims on pargasites; and (3) a "high shear zone" with strongly aligned tabular microlites, significantly collapsed pores and thick granular reaction rims on pargasite microlites. Using the temperature profile monitored across the shear zone by the thermographic camera, we can estimate the temperature range at which each of these discrete zones (and textures) would have formed (Fig. 13a), with the low shear zone between 790–860 ºC, moderate shear zone between 860–980 ºC and high shear zone between 980–1080 ºC, with any bulk melting taking place at >1100 ºC.

INTERPRETATION AND DISCUSSION

Direct field studies investigating the textural complexities associated with extruding lavas are in short supply due to the prolonged, ongoing nature of lava dome eruptions, in addition to the low probability that extruded structures remain well enough preserved to interpret the processes involved effectively (Mount St. Helens – e.g. Pallister *et al*. 2013; Gaunt *et al*. 2014; Unzen volcano – e.g. Smith *et al.*, 2001; Volcán de Colima – e.g. Kendrick *et al.*, 2016; Cordón Caulle – e.g. Castro *et al*., 2013; Tuffen *et al.*, 2013). The quiescence following the 1991–1995 dome-building eruption at Unzen volcano provided this unique opportunity, where remnants of the extruded lava spine and associated marginal shear zones remain intact.

Strain localisation and viscous remobilisation

Our observations suggest the formation of these shear zones were a consequence of strain localisation, which in turn was governed by changes in the magma's rheology during its ascent to the surface. Late-stage crystallisation and degassing of the dacitic magma (e.g. Noguchi *et al.*, 2008b; Cichy *et al.*, 2011) would increase viscosity and significantly hamper flow in the conduit, aiding a rheological transition of the magma, causing stress and strain to localise near the conduit margins (Fig. 14 panel [1]). A concentration of stress in the high viscosity, crystal-rich magma likely led to the dissipation of viscous energy (shear heating) or friction resulting in a temperature rise (e.g. Lavallée *et al.*, 2008; Kendrick *et al.*, 2014b), which reduced the viscosity of the magma allowing crystals to align in the direction of flow (i.e. viscously remobilise; Fig. 6b), and pores to compact (Figs 5, 6a–c) reducing permeability (e.g. Kendrick *et al.*, 2014a; Ashwell *et al.*, 2015). The presence of an interstitial glass facilitates viscous remobilisation (e.g. Hornby *et al.*, 2015); when a glass is not present, for example at Mount St. Helens, lava spines extrude in a near-solid state with no high-temperature deformation of this kind observed (Cashman *et al.*, 2008; Kennedy *et al.*, 2009;

Kendrick *et al.*, 2012; Pallister *et al.*, 2013; Ryan *et al.*, 2018). Here, the interstitial glass presents an opportunity to constrain the likely conditions during spine extrusion based on textural evolution, which indicates increasing temperature towards the spine margin (i.e. high shear zone). As experimentally demonstrated here (Fig. 13a and f), viscous remobilisation and subsequent crystal rotation and alignment likely took place 200–300 ºC degrees above T_g (980–1080 ºC). Our experiment also constrains an estimated temperature at which the magma in the conduit would remain undeformed (i.e. low shear zone), likely reflecting the temperature of the magma that formed the core of the spine (~860 ºC, Fig. 13f), which is in close agreement to the post-magma mixing temperatures previously reported (870–900 ºC; Venezky & Rutherford, 1999; Holtz *et al.*, 2005).

Thermal destabilisation of amphibole

A characteristic effect of disequilibrium conditions is the reaction of mineral phases with the surrounding melt. Hydrous minerals, such as amphibole, are sensitive recorders of such processes and once forced out of their stability zone begin to break down, forming a rim of anhydrous phases (e.g. Rutherford & Hill, 1993; Browne & Gardner, 2006; De Angelis *et al.*, 2015). Although many factors can cause amphibole decomposition (e.g. decompression, heating, change in melt chemistry, oxidation; Rutherford & Hill, 1993), we investigate the effect of shearing on the dynamic stability of amphibole during magma ascent at Unzen volcano. Within the sheared margins of the lava spine, high-temperature flow appears to influence the stability of pargasitic amphibole, causing localised breakdown rims (Fig. 11a). The granular rims are exclusive to the high shear zone and gouge material, often surrounding a symplectitic rim. The symplectitic rims are always in direct contact with pargasite crystals and found across the entire shear zone with varying thickness (Fig. 11a). Thus, based on the theoretical understanding of reaction rims growing from the outer edge of the crystal inwards

towards the centre (e.g. Browne & Gardner, 2006), the granular rims formed first followed by symplectitic decay. Experimental investigations on heating-induced amphibole reaction rims (De Angelis *et al.*, 2015) are texturally comparable to the granular rims observed in the high shear and gouge regions of the spine. Shear heating in these areas is the likely process that could cause the pargasite to break down, occurring contemporaneously with crystal alignment and pore compaction (Fig. 14 panel [2]). Similar granular rims also formed during the rotary shear experiment, owing to a localised temperature rise brought about by frictional and shear heating (Fig. 13g and h). Symplectitic rims (Fig. 11a) have previously been related to extreme oxidation (i.e. at shallow conditions; Garcia & Jacobson, 1979); however, these textures have been recorded at other lava domes, being located as patches, either on the outer edge of a granular rim (Plechov *et al.*, 2011) or between the granular rim and the host amphibole (Scott *et al.*, 2012), making oxidation inconclusive. Yet, owing to the slow extrusion and cooling of the dacitic spine (Nakada & Motomura, 1999), along with the visual observation of surface reddening across outcrop 1 (Fig. 2a) and in blocks on the dome (e.g. Saito *et al.*, 2007), it may imply that the symplectitic rims were the result of late-stage oxidation (e.g. Murphy *et al.*, 2000). Kinetic variations across the shear zone also need to be taken into account due to a localised heat input related to shearing near the spine margin, with symplectitic rims possibly reflecting a kinetic delay (e.g. Scott *et al.*, 2012). Less kinetic inhibition would be expected near the spine margin, leading to the formation of coarser grained reaction rims. However, the coexistence of granular and symplectitic rims on the same pargasite crystal suggests two discrete events were responsible; heating exclusive to the high shear zone, followed by shallower oxidation of the shear zone as a whole (Fig. 14 panel [3]).

Crystal plasticity as a strain indicator

As magma approaches the viscous-brittle transition, flow behaviour converts from magmatic, viscous flow to near solid-state where fracturing and internal crystal deformation is feasible (Vernon, 2000). Solid-state crystal deformation has been observed to superimpose magmatic flow textures in several plutonic bodies (Murray, 1979; Vernon & Paterson, 1993; Zibra *et al.*, 2012). Typically, eruptive products lack these microstructural textures due to the sustained coexistence of a melt fraction, which may relax stress by adapting to new configurations. However, we show that crystals in magmatic shear zones do not only interact by acting as rigid, brittle bodies, but can serve to accommodate strain by deforming plastically and that this plasticity varies systematically with deformation conditions before succumbing to failure. The presence of these deformation textures may be attributed to the low interstitial melt concentrations and the prolonged timescales of magma ascent (~5 months), allowing more time for the crystals to capture the transition from viscous to brittle behaviour. Kendrick *et al.* (2017) experimentally induced plastic deformation within plagioclase microlites present in an andesitic dome lava (from Volcán de Colima, Mexico), highlighting that microlites that were subjected to higher stresses and strains had a higher misorientation (i.e. internal lattice distortion), akin to the systematic variation recorded here across the shear zone of the spine. The increase in crystal plasticity of plagioclase microlites (Fig. 9a–d) suggests more stress and strain was localised and accommodated in these areas (Fig. 14 panel [3]). This is further confirmed by the extreme plastic deformation of biotite phenocrysts in the high shear zone (Fig. 8b and c), which are akin to mica "fish" associated with S-C fabrics within mylonitic shear zones in fully crystalline rocks (e.g. Selverstone *et al.*, 2012). It has been observed that yield stresses required for plasticity to initiate decrease with increasing temperature (Poirier, 1995). Therefore, a higher stress and strain at the conduit margins (e.g. Cordonnier *et al.*, 2009; Lavallée *et al.*, 2012b; Lavallée *et al.*, 2013),

accompanied by a thermal input due to shear heating and fault friction, would facilitate the observed increase in crystal plasticity towards the spine margin. Additionally, temperature increase could cause a crystal plasticity feedback mechanism, as increasing temperatures would lower the viscosity of the magma in the higher shear zone, enabling further strain to localise and favour yet higher crystal plastic deformation in this region. With more experimentation, building on the work of Kendrick *et al.* (2017), the strain rates required to achieve plastic deformation and failure in different phases could be quantified and thus incorporated into future rheological models.

Brittle failure and comminution

During spine extrusion, and once in the transitional brittle regime, crystals can fracture and comminute in areas of higher stress, resulting in a net grain size reduction of phenocrysts towards the spine margins (Fig. 14 panel [4]). The cataclastic behaviour, dominantly of plagioclase and amphibole phenocrysts (Fig. 4 and 7a), can thus be attributed to brittle deformation during fault slip (e.g. Monzawa & Otsuki, 2003). The point at which brittle failure would take over from viscous and plastic deformation depends on both the temperature and stress (and strain) conditions of the magma (e.g. Allen & McPhie, 2003; Lavallée *et al.*, 2008; Cordonnier *et al.*, 2009; Cordonnier *et al.*, 2012). Similar brittle textures were observed following uniaxial compression experiments performed on 80 mm by 40 mm cores of natural Unzen dacite at 980 ºC, 1–32 MPa applied normal stress and total strain of 25 % (Cordonnier *et al.*, 2009). These experiments showed that with increasing stress, phenocrysts first cracked, then began to fragment to reduce grain size gradually, and at highest stresses crystal powders formed, with plagioclase and amphibole phenocrysts being the most affected. The decrease in plagioclase circularity in the higher shear zone (sample B, Fig. 7b) can be related to initial

remobilisation and preferential alignment of the crystals during shear, and subsequent fracturing parallel to the principle shear direction.

Cordonnier *et al.* (2009) reported that following deformation of Unzen lavas under high stresses, finer crystal fragments and powders were commonly removed during thin section preparation, leaving behind voids with some residual fragments remaining. This is in keeping with our observations that increasing comminution of plagioclase and, to a lesser extent, amphibole caused their systematic reduction in size and abundance due to higher stress conditions at the spine margin (Fig. 2c, d, and Table 2). Biotite phenocrysts show no such reduction in abundance owing to their ability to deform plastically (Fig. 8c and d) and remain cohesive within the high shear zone and gouge. These differences in a crystal's mechanical response to shear may be a partial cause (along with natural heterogeneities) for the subtle variability in bulk-rock major and trace elements across the shear zone (Table 1); for example, the drop in plagioclase compatible elements (Sr, Ca, Na, Al) in the high shear zone relative to the low shear zone is consistent with the reduction of plagioclase recorded by QEMSCAN. It is also likely that the conduit wall-rock underwent some degree of fracturing, contributing material (along with the high shear zone) to the gouge, and thus causing a further variability in mineralogy (Fig. 4, Tables 1 and 2).

Brittle deformation within the conduit margin shear zones is believed to be the cause of the characteristic seismicity (Fig. 14) recorded during spine extrusion (Tuffen & Dingwell, 2005; Iverson *et al.*, 2006; Neuberg *et al.*, 2006; Iverson, 2008; Kendrick *et al.*, 2014b; Hornby *et al.*, 2015; Lamb *et al.*, 2015). The depth of the seismic source during spine extrusion at Unzen volcano was constrained to be <500 m (Yamashina *et al.*, 1999; Umakoshi *et al.*, 2008; Lamb *et al.*, 2015), thus the onset of brittle deformation is estimated to occur at a similar depth, perhaps superseding viscous and crystal-plastic behaviour at this depth.

Continued fracturing at the conduit margins caused faulting to extend to the surface, allowing the magma to extrude in the form of a lava spine, mantled by cataclastic gouge material.

Magnetic response to shear

Magnetic properties of rocks can be highly sensitive to magneto-mineralogical changes brought about by, for example, deformation and faulting generating heat (Ben-Zion & Sammis, 2003; Ferré *et al.*, 2005; Freund *et al.*, 2007; Kendrick *et al.*, 2012) or hydrothermal alteration due to flushing through of fluids or gases (Krása & Herrero-Bervera, 2005; Bouligand *et al.*, 2014; Geuna *et al.*, 2014). The magnetic variations across the spine shear zone reveal a disparate history of the magnetic carriers that coincide with the degree of shear. The variation in the reversibility of the magnetic susceptibility curves (Fig. 10d) suggests a single, low coercivity phase of low-Ti titanomagnetite (T_C ~530 °C) in the host material; the less reversible curves of the high shear zone and gouge indicate a more distributed range of less stable phases, perhaps with suppressed Curie temperatures. The almost full saturation of the IRM and backfield curves support the predominance of these low coercivity minerals (Leonhardt, 2006). However, the higher T_C, B_{cr}, M_{rs}/M_s and B_c values in the gouge (Table 3 and Fig. 10e) suggests an increasing fraction of higher coercivity magnetite grains. These were likely produced by oxidation of the titanomagnetite in the gouge either through subdividing them further into lamellae of iron-rich and iron-poor end members (i.e. oxyexsolution), or potentially even via conversion to titanohaematite. Interestingly, the undeformed host material consistently plots between the high shear zone and gouge (Fig. 10e and g), suggestive of two opposing formation pathways that took place at the spine margin. One event, likely oxidation well above ambient temperatures, influenced the high shear zone and gouge to differing degrees, creating the spread in susceptibility and coercivity ratio (Fig. 10a–g). However, the high shear appears to have been influenced by a second factor,

potentially a pre- or syn-emplacement re-heating event that shifted the coercive force, and hence domain state in the opposite manner to the gouge (Fig. 10e and g). Such a shift in the magnetic carriers could be the result of shear or frictional heating in the laterally limited high shear zone (Fig. 3a).

Gouge alteration and glass devitrification

The low porosity of the glass-poor gouge relative to the least sheared region of the spine suggests that extensive induration of the plastically deformed and comminuted crystal fragments took place (Fig. 2b and 4), which would be facilitated by the increased temperatures and stress conditions at the conduit margin (e.g. Ryan *et al.*, 2018). However, during its formation and lithification, the gouge is envisaged to have been exposed to prolonged periods of fluid and gas interaction, particularly during slow extrusion and post-emplacement degassing, causing alteration which is visible in outcrop scale due to the red colouration of the gouge (Figs 2b and 3b). The groundmass silica phase within the gouge is somewhat comparable to that found in drilled dacitic dykes retrieved by the USDP-4 Unzen Scientific Drilling Project (Fig. 11a; Noguchi *et al.*, 2008a), although the gouge lacks evidence for other alteration phases (e.g. pyrite and alkali-feldspar). One of these dykes (dyke C14) has been interpreted to be the feeder dyke for the 1991–1995 eruption based on its similar texture and composition to the erupted dome lava, but with a distinct overprint of a mosaic of silica-rich grains in the groundmass attributed to hydrothermal alteration by percolating fluids (Noguchi *et al.*, 2008a). Therefore, in addition to the significant difference in rock magnetic parameters of the gouge (susceptibility and coercivity ratio; Fig. 10d and e), this suggests the gouge layer experienced increased interaction with percolating hydrothermal fluids/gases relative to the bulk of the magma in the conduit. Fluids and gases filtrating through magmas and rocks have been seen to influence many petrological, geochemical and

magnetic parameters in volcanic systems (e.g. Krása & Herrero-Bervera, 2005; Salaun *et al.*, 2011; Bouligand *et al.*, 2014; Geuna *et al.*, 2014). Chemical effects are the result of transport of dissolved species either by diffusion or percolating fluids through open pores (Goncalves *et al.*, 2012). Metasomatism of this kind has been observed in many large-scale shear zones (e.g. Wibberley, 1999; Yonkee *et al.*, 2013) thus deciphering the influence of fluid migration during spine extrusion is critical. Porosity measurements (Table 2 and Fig. 5) across the shear zone reveal a decrease from low shear to high shear, resulting from pervasive compaction in the shear zone occurring at depth. The prevention of fluid access with increasing shear-enhanced compaction would aid in the relative stabilisation of mineral phases, preventing geochemical reactions from taking place (e.g. Wibberley, 1999).

Devitrification of amorphous glass is a common feature observed in many dome lavas (e.g. Mount St. Helens, Pallister *et al.*, 2008; Santiaguito, Scott *et al.*, 2012; Soufrière Hills volcano, Horwell *et al.*, 2013); this is a solid-state crystallisation process that takes place during the slow cooling of the magma, leading to the formation of crystalline silica (SiO_2) phases, commonly cristobalite (e.g. Baxter *et al.*, 1999; Murphy *et al.*, 2000; Horwell *et al.*, 2013). Partially devitrified glass has previously been reported in the Unzen lava spine by Nakada & Motomura (1999). The presence of groundmass SiO_2 microlites in the shear zone, increasing systematically towards the spine exterior (Fig. 11a), are likely devitrification products, consistent to those textures observed in other systems (Cashman, 1992; Blundy & Cashman, 2001; Couch *et al.*, 2003; Harford *et al.*, 2003; Horwell *et al.*, 2013). Decompression experiments (Hammer & Rutherford, 2002; Couch *et al.*, 2003) observed similar devitrification textures forming only at very low pressures (≤5 MPa), which led to the proposal that the extent of devitrification could act as a relative estimate for extrusion rate (Scott *et al.*, 2012; Horwell *et al.*, 2013), with increased devitrification during slower extrusion. Thus, devitrification of the spine is consistent with its low extrusion rate and slow

cooling (Nakada & Motomura, 1999), and likely coincided with oxidation and the formation of symplectitic rims on pargasite microlites. The high shear zone glass (representing the margin of the spine) is slightly more devitrified (Fig. 11a), which could reflect the higher temperatures experienced associated with shear that prolonged the cooling period to ambient temperature and consequently influenced the glass chemistry (Fig. 12). This is further supported by the higher abundance of more evenly distributed groundmass silica phases in the gouge (Fig. 11a), which may have spent a relatively longer amount of time in the conduit than the bulk of the spine due to periodic coupling to the conduit wall.

Magma mixing: An added complexity

Evidence for magma mixing is common in the eruptive products at Unzen volcano (e.g. Nakada & Fujii, 1993; Nakamura, 1995; Nakada & Motomura, 1999; Venezky & Rutherford, 1999), including the spine (e.g. biotite reaction rims, mafic enclaves). Pre- and syn-eruptive magma mixing has been documented at other volcanoes, leaving behind petrological and geochemical signatures (e.g. reaction rims on hydrous minerals, reverse zoning, and changes in bulk and glass composition). This brings complications when deciphering the impact of shear and the natural heterogeneities brought about by mixing of the magmas at depth. For example, reaction rims on amphiboles have previously been related to a temperature rise brought about by mixing a lower temperature and higher temperature magma (e.g. Murphy *et al.*, 2000; Rutherford & Devine, 2003; De Angelis *et al.*, 2015). This could be an alternative cause for the pargasite rims observed in the spine shear zone. Additionally, magma mixing can bring about hybridised, compositional heterogeneities in both major and trace elements (e.g. Perugini & Poli, 2012; Morgavi *et al.*, 2013), which could explain the subtle differences in bulk-rock composition across the shear zone. However, magma mixing is deemed an unsystematic, chaotic process; thus, although mixing of two or more magmas could explain

the aforementioned differences across the shear zone, their systematic change with shear intensity and the range of complementary deformation indicators suggests otherwise. It has also been suggested that mixing of the magma at Unzen would be near-complete prior to reaching the last kilometre before extrusion (Nakada & Motomura, 1999; Goto *et al.*, 2008), while here we demonstrate that the differences observed across the spine shear zone likely formed within the final kilometre, and thus on a fully mixed magma. Nakada & Motomura (1999) found the bulk-rock composition of the porphyritic dacites from pyroclastic flow deposits collected throughout the 4-year eruption ranged from 64.5–66.0 wt % SiO_2, which was related to the natural variation in the abundance of phenocrysts. Consequently, although it is possible to attribute some of the bulk geochemical and mineralogical differences across the shear zone to deformation (fracturing of crystals during magma ascent and some loss of finer fragments forming cavities), inherent variabilities in the magma are expected. Therefore, it is important to consider, particularly for geochemical interpretations, natural variabilities within a mixed magma and refrain from over-interpretation of subtle differences.

IMPLICATIONS FOR ERUPTION STYLE

Shear deformation and strain localisation in the volcanic conduit can regulate eruptive behaviour as demonstrated by the range of characteristic textures that record shallow conduit processes. We relate the combined effect of viscous remobilisation, pore compaction, pargasite destabilisation and variations in magnetic properties to a magmatic heating episode near the conduit margins as a consequence of shearing and friction during magma ascent, manifested here primarily in the high shear zone (see Fig. 14). This was likely followed by late fluid-rock alteration, oxidation and glass devitrification of the gouge and, to a lesser extent, high shear regions of the spine.

In volcanic systems, highly fractured materials that reside in the conduit are ideal permeable pathways that facilitate outgassing, and thus reduce explosive potential (e.g. Gaunt *et al.*, 2014; Ashwell *et al.*, 2015; Lamur *et al.*, 2017). Marginal shear zones with their increased permeable network resulting from fracturing are believed to contribute to such depressurisation, preventing the build-up of excess pressure that can drive explosivity. However, within the shear zone examined here, localised compaction of the magma brought about by an increased temperature resulted in a closure of the original porous network and reduced permeability in these zones. As outgassing proficiency depends on the pore connectivity and permeability anisotropy of the undeformed magma (e.g. Ashwell *et al.*, 2015; Heap *et al.*, 2015; Farquharson *et al.*, 2016; Colombier *et al.*, 2017; Gonnermann *et al.*, 2017; Lamur *et al.*, 2017), the compaction and closure of pore space in the high shear zone could have caused a shift in the location of outgassing, in this case towards the least sheared material (i.e. the core of the spine). A dilemma, therefore, arises when assessing a magma's ability to fracture (i.e. dilate) or compact in shear zones (Heap *et al.*, 2015), with the competition between the two favouring or limiting the extent of outgassing and therefore likely regulating the style of eruption. For example, explosive activity at Santiaguito volcano, Guatemala, has been attributed to strain localisation and faulting at the conduit margins (Lavallée *et al.*, 2015), creating a partially open-vent system that regularly seals to build pressure that produces an explosion (Holland *et al.*, 2011; Johnson *et al.*, 2014). Although during the 1991–1995 eruption no explosive activity was reported, likely owing to a sufficient connectivity of the magma's degassing network (Nakada & Motomura, 1999; Nakada *et al.*, 1999), this may not be the case for other systems or throughout any other given eruption where shifts from effusive–explosive activity have been observed (Cassidy *et al.*, 2018). Our model suggests magma shearing at the conduit margin could temporally seal gas pathways, by compacting the porous network, creating ideal conditions for explosive activity, a

phenomenon that may also be responsible for the frequent shifts in eruption style observed at many other dome-building volcanoes (Voight *et al.*, 1999; Mason *et al.*, 2006; Clarke *et al.*, 2007; Lensky *et al.*, 2008; Michaut *et al.*, 2009; Kennedy *et al.*, 2010; Ashwell *et al.*, 2015; Farquharson *et al.*, 2016; Heap *et al.*, 2017). Petrological evidence for such a process influencing eruption style may be found in explosive deposits (i.e., ash and bombs); such signatures may include a combination of poorly vesicular clasts accompanied by plastically deformed microlites that show a fluidal or strong alignment, and in extreme cases the appearance of frictional melts.

CONCLUDING STATEMENT

In this study, we integrated multidisciplinary observations made through field examinations, petrology, microstructures, crystallography, magnetics and experimentation, to constrain the impact of shear on the petrological evolution of magma during ascent and spine extrusion at Unzen volcano, Japan. Our results show that crystals can act as an outlet for strain via crystal plasticity, leading the magma towards failure, thus effectively monitoring stress conditions. This accumulation of strain coincides with disequilibrium conditions in the conduit, assisting in mineral decomposition, alteration, crystal alignment, and pore compaction, owing to shear heating near the margin during the late-stages of spine extrusion. This process is overprinted, perhaps by increasing prevalence of dilational shear in the upper conduit, by a narrow gouge layer, characterised by distinct petrographic and magnetic properties typical of gas- or fluid-flushing induced alteration, which influences the neighbouring compactional high shear zone to a lesser extent. These deformation microstructures and related processes envisaged in the shallow conduit, especially during the ascent of high viscosity magma, can have a significant effect on the permeability network, altering the degassing efficiency and extent of fluid-magma interaction during magma ascent, ultimately controlling the style of eruption seen at

the surface. For this reason, incorporation of these late-stage processes (i.e. shear heating, crystal plasticity, shear-induced mineral reactions and comminution) into rheological models may assist in constraining the complexities associated with on-going eruptions and thus aid in our understanding of shifts from effusive to explosive activity.

FUNDING

This work was financially supported by a European Research Council Starting Grant on 'Strain Localisation in Magmas' (SLiM, grant number 306488). Fieldwork in summer 2016 was supported by a Daiwa Anglo-Japanese Foundation Award. J.E. Kendrick was funded by an Early Career Fellowship of the Leverhulme Trust. EBSD analyses were undertaken in the EBSD-SEM Laboratory at the University of Liverpool and were supported by funding to E. Mariani.

AKNOWLEDGMENTS

We would like to thank FEI Company of Hilsboro Oregon, and R. Worden of the University of Liverpool, for the support with QEMSCAN data collection. We also thank H. Shimizu for his continued support during field excursions in 2013 and 2016. Thanks to T. Knott for XRF measurements and J. Wade and P. Gopon for technical assistance with the electron probe microanalysis. We wish to thank the editor, W. Bohrson, and reviewers L. Caricchi and M. Rowe, for their detailed and constructive reviews.

SUPPLEMENTARY DATA

Supplementary figures (Fig. S1–S9) and Electronic Appendices (1–3) are available from *Journal of Petrology* online http://www.petrology.oxfordjournals.org.

REFERENCES

Allen, S. R. & McPhie, J. (2003). Phenocryst fragments in rhyolitic lavas and lava domes. *Journal of Volcanology and Geothermal Research* **126**, 263–283.

Ashwell, P. A., Kendrick, J. E., Lavallée, Y., Kennedy, B. M., Hess, K. U., von Aulock, F. W., Wadsworth, F. B., Vasseur, J. & Dingwell, D. B. (2015). Permeability of compacting porous lavas. *Journal of Geophysical Research: Solid Earth* **120**, 1605–1622.

Ayling, B., Rose, P., Petty, S., Zemach, E. & Drakos, P. (2012). QEMSCAN (quantitative evaluation of minerals by scanning electron microscopy): capability and application to fracture characterization in geothermal systems. *Thirty-Seventh Workshop on Geothermal Reservoir Engineering*. Stanford, California, USA, 30 January–1 February, 2012.

Baxter, P. J., Bonadonna, C., Dupree, R., Hards, V. L., Kohn, S. C., Murphy, M. D., Nichols, A., Nicholson, R. A., Norton, G., Searl, A., Sparks, R. S. J. & Vickers, B. P. (1999). Cristobalite in Volcanic Ash of the Soufriere Hills Volcano, Montserrat, British West Indies. *Science* **283**, 1142–1145.

Ben-Zion, Y. & Sammis, C. G. (2003). Characterization of Fault Zones. *Pure and Applied Geophysics* **160**, 677–715.

Bloemendal, J., King, J. W., Hall, F. R. & Doh, S. J. (1992). Rock Magnetism of Late Neogene and Pleistocene Deep-Sea Sediments: Relationship to Sediment Source, Diagenetic Processes, and Sediment Lithology. *Journal of Geophysical Research* **97**, 4361–4375.

Blundy, J. & Cashman, K. (2001). Ascent-driven crystallisation of dacite magmas at Mount St Helens, 1980-1986. *Contributions to Mineralogy and Petrology* **140**, 631–650.

Bouligand, C., Glen, J. M. G. & Blakely, R. J. (2014). Distribution of buried hydrothermal alteration deduced from high-resolution magnetic surveys in Yellowstone National Park. *Journal of Geophysical Research: Solid Earth* **119**, 2595–2630.

Brewer, L. N., Othon, M. A., Young, L. M. & Angeliu, T. M. (2006). Misorientation mapping for visualization of plastic deformation via electron back-scattered diffraction. *Microscopy and Microanalysis* **12**, 85–91.

Browne, B. L. & Gardner, J. E. (2006). The influence of magma ascent path on the texture, mineralogy, and formation of hornblende reaction rims. *Earth and Planetary Science Letters* **246**, 161–176.

Caricchi, L., Burlini, L., Ulmer, P., Gerya, T., Vassalli, M. & Papale, P. (2007). Non-Newtonian rheology of crystal-bearing magmas and implications for magma ascent dynamics. *Earth and Planetary Science Letters* **264**, 402–419.

Carslaw, H. S. & Jaeger, J. C. (1959). *Conduction of heat in solids*. Oxford,: Clarendon Press.

Cashman, K. V. (1992). Groundmass Crystallization of Mount St Helens Dacite, 1980-1986 - a Tool for Interpreting Shallow Magmatic Processes. *Contributions to Mineralogy and Petrology* **109**, 431–449.

Cashman, K. V. & Sparks, R. S. J. (2013). How volcanoes work: A 25 year perspective. *Geological Society of America Bulletin* **125**, 664–690.

Cashman, K. V., Thornber, C. R. & Pallister, J. S. (2008). From Dome to Dust: Shallow Crystallization and Fragmentation of Conduit Magma During the 2004-2006 Dome Extrusion

of Mount St. Helens, Washington. In: Sherrod, D. R., Scott, W. E. & Stauffer, P. H. (eds.) *A Volcano Rekindled: The Renewed Eruption of Mount St. Helens, 2004-2006. Professional Paper 1750.*: U.S. Geological Survey, 387–413.

Cassidy, M., Manga, M., Cashman, K. & Bachmann, O. (2018). Controls on explosive-effusive volcanic eruption styles. *Nature Communications* **9**, 2839.

Castro, J., Schipper, C. I., Mueller, S. P., Militzer, A. S., Amigo, A., Parejas, C. S. & Jacob, D. (2013). Storage and eruption of near-liquidus rhyolite magma at Cordón Caulle, Chile. *Bulletin of Volcanology* **75**, 1–17.

Cichy, S. B., Botcharnikov, R. E., Holtz, F. & Behrens, H. (2011). Vesiculation and Microlite Crystallization Induced by Decompression: a Case Study of the 1991-1995 Mt Unzen Eruption (Japan). *Journal of Petrology* **52**, 1469–1492.

Clarke, A. B., Stephens, S., Teasdale, R., Sparks, R. S. J. & Diller, K. (2007). Petrologic constraints on the decompression history of magma prior to Vulcanian explosions at the Souffiere Hills volcano, Montserrat. *Journal of Volcanology and Geothermal Research* **161**, 261–274.

Coats, R., Kendrick, J. E., Wallace, P. A., Miwa, T., Hornby, A. J., Ashworth, J. D., Matsushima, T. & Lavallée, Y. (2018). Failure criteria for porous dome rocks and lavas: a study of Mt. Unzen, Japan. *Solid Earth* **9**, 1299–1328.

Colombier, M., Wadsworth, F. B., Gurioli, L., Scheu, B., Kueppers, U., Muro, A. D. & Dingwell, D. B. (2017). The evolution of pore connectivity in volcanic rocks. *Earth and Planetary Science Letters* **462**, 99–109.

Cordonnier, B., Caricchi, L., Pistone, M., Castro, J., Hess, K.-U., Gottschaller, S., Manga, M., Dingwell, D. B. & Burlini, L. (2012). The viscous-brittle transition of crystal-bearing silicic melt: Direct observation of magma rupture and healing. *Geology* **40**, 611–614.

Cordonnier, B., Hess, K.-U., Lavallée, Y. & Dingwell, D. B. (2009). Rheological properties of dome lavas: Case study of Unzen volcano. *Earth and Planetary Science Letters* **279**, 263–272.

Costa, A. & Macedonio, G. (2003). Viscous heating in fluids with temperature-dependent viscosity: implications for magma flows. *Nonlinear Processes in Geophysics* **10**, 545–555.

Costa, A., Melnik, O. & Vedeneeva, E. (2007). Thermal effects during magma ascent in conduits. *Journal of Geophysical Research: Solid Earth* **112**.

Couch, S., Harford, C. L., Sparks, R. S. J. & Carroll, M. R. (2003). Experimental constraints on the conditions of formation of highly calcic plagioclase microlites at the Soufrire Hills Volcano, Montserrat. *Journal of Petrology* **44**, 1455–1475.

Day, R., Fuller, M. & Schmidt, V. A. (1977). Hysteresis properties of titanomagnetites: Grain-size and compositional dependence. *Physics of the Earth and Planetary Interiors* **13**, 260–267.

De Angelis, S. H., Larsen, J., Coombs, M., Dunn, A. & Hayden, L. (2015). Amphibole reaction rims as a record of pre-eruptive magmatic heating: An experimental approach. *Earth and Planetary Science Letters* **426**, 235–245.

Deubelbeiss, Y., Kaus, B. J. P., Connolly, J. A. D. & Caricchi, L. (2011). Potential causes for the non-Newtonian rheology of crystal-bearing magmas. *Geochemistry, Geophysics, Geosystems* **12**, Q05007.

Dingwell, D. & Webb, S. L. (1989). Structural relaxation in silicate melts and Non-Newtonian melt rheology in geologic processes. *Physics and Chemistry of Minerals* **16**, 508–516.

Dunlop, D. J. (2002). Theory and application of the Day plot (Mrs/Ms versus Hcr/Hc) 1. Theoretical curves and tests using titanomagnetite data. *Journal of Geophysical Research* **107**, 2056.

Fabian, K. (2003). Some additional parameters to estimate domain state from isothermal magnetization measurements. *Earth and Planetary Science Letters* **213**, 337–345.

Farquharson, J. I., Heap, M. J., Lavallee, Y., Varley, N. R. & Baud, P. (2016). Evidence for the development of permeability anisotropy in lava domes and volcanic conduits. *Journal of Volcanology and Geothermal Research* **323**, 163–185.

Ferré, E. C., Zechmeister, M. S., Geissman, J. W., MathanaSekaran, N. & Kocak, K. (2005). The origin of high magnetic remanence in fault pseudotachylites: Theoretical considerations and implication for coseismic electrical currents. *Tectonophysics* **402**, 125–139.

Forien, M., Arbaret, L., Burgisser, A. & Champallier, R. (2011). Experimental constrains on shear-induced crystal breakage in magmas. *Journal of Geophysical Research: Solid Earth* **116**.

Freund, F., Salgueiro da Silva, M. A., Lau, B. W. S., Takeuchi, A. & Jones, H. H. (2007). Electric currents along earthquake faults and the magnetization of pseudotachylite veins. *Tectonophysics* **431**, 131–141.

Garcia, M. & Jacobson, S. (1979). Crystal clots, amphibole fractionation and the evolution of calc-alkaline magmas. *Contributions to Mineralogy and Petrology* **69**, 319–327.

Gaunt, H. E., Sammonds, P. R., Meredith, P. G., Smith, R. & Pallister, J. S. (2014). Pathways for degassing during the lava dome eruption of Mount St. Helens 2004–2008. *Geology* **42**, 947–950.

Geuna, S. E., Lagorio, S. L. & Vizán, H. (2014). Oxidation processes and their effects on the magnetic remanence of Early Cretaceous subaerial basalts from Sierra Chica de Córdoba, Argentina. *Geological Society, London, Special Publications* **396**, 239–263.

Giordano, D., Russell, J. K. & Dingwell, D. B. (2008). Viscosity of magmatic liquids: A model. *Earth and Planetary Science Letters* **271**, 123–134.

Goncalves, P., Oliot, E., Marquer, D. & Connolly, J. A. D. (2012). Role of chemical processes on shear zone formation: an example from the Grimsel metagranodiorite (Aar massif, Central Alps). *Journal of Metamorphic Geology* **30**, 703–722.

Gonnermann, H. M., Giachetti, T., Fliedner, C., Nguyen, C. T., Houghton, B. F., Crozier, J. A. & Carey, R. J. (2017). Permeability During Magma Expansion and Compaction. *Journal of Geophysical Research: Solid Earth* **122**, 9825–9848.

Goto, Y., Nakada, S., Kurokawa, M., Shimano, T., Sugimoto, T., Sakuma, S., Hoshizumi, H., Yoshimoto, M. & Uto, K. (2008). Character and origin of lithofacies in the conduit of Unzen volcano, Japan. *Journal of Volcanology and Geothermal Research* **175**, 45–59.

Gottlieb, P., Wilkie, G., Sutherland, D., Ho-Tun, E., Suthers, S., Perera, K., Jenkins, B., Spencer, S., Butcher, A. & Rayner, J. (2000). Using quantitative electron microscopy for process mineralogy applications. *Journal of the Minerals, Metals & Materials Society* **52**, 24–25.

Hale, A. J. (2007). Magma flow instabilities in a volcanic conduit: Implications for long-period seismicity. *Physics of the Earth and Planetary Interiors* **163**, 163–178.

Hale, A. J. & Wadge, G. (2008). The transition from endogenous to exogenous growth of lava domes with the development of shear bands. *Journal of Volcanology and Geothermal Research* **171**, 237–257.

Hale, A. J., Wadge, G. & Muhlhaus, H. B. (2007). The influence of viscous and latent heating on crystal-rich magma flow in a conduit. *Geophysical Journal International* **171**, 1406–1429.

Hammer, J. E. & Rutherford, M. J. (2002). An experimental study of the kinetics of decompression-induced crystallization in silicic melt. *Journal of Geophysical Research: Solid Earth* **107**.

Harford, C. L., Sparks, R. S. J. & Fallick, A. E. (2003). Degassing at the Soufrière Hills Volcano, Montserrat, recorded in matrix glass compositions. *Journal of Petrology* **44**, 1503–1523.

Hayman, N. W., Housen, B. A., Cladouhos, T. T. & Livi, K. (2004). Magnetic and clast fabrics as measurements of grain-scale processes within the Death Valley shallow crustal detachment faults. *Journal of Geophysical Research: Solid Earth* **109**.

Heap, M. J., Farquharson, J. I., Baud, P., Lavallee, Y. & Reuschle, T. (2015). Fracture and compaction of andesite in a volcanic edifice. *Bulletin of Volcanology* **77**, 55.

Heap, M. J., Violay, M., Wadsworth, F. B. & Vasseur, J. (2017). From rock to magma and back again: The evolution of temperature and deformation mechanism in conduit margin zones. *Earth and Planetary Science Letters* **463**, 92–100.

Hendrasto, M., Eto, T., Kimata, F., Matsushima, T. & Ishihara, K. (1997). Magma transport at Mt. Unzen associated with the 1990–1995 activity inferred from levelling data. *Disaster Prevention Research Institute Annuals* **40**, 61–72.

Henkel, O. (1964). Remanenzverhalten und Wechselwirkungen in hartmagnetischen Teilchenkollektiven. *physica status solidi (b)* **7**, 919–929.

Hess, K.-U., Cordonnier, B., Lavallée, Y. & Dingwell, D. B. (2008). Viscous heating in rhyolite: An in situ experimental determination. *Earth and Planetary Science Letters* **275**, 121–126.

Hirose, T. & Shimamoto, T. (2005). Growth of molten zone as a mechanism of slip weakening of simulated faults in gabbro during frictional melting. *Journal of Geophysical Research: Solid Earth* **110**, B05202.

Holland, A. S. P., Watson, I. M., Phillips, J. C., Caricchi, L. & Dalton, M. P. (2011). Degassing processes during lava dome growth: Insights from Santiaguito lava dome, Guatemala. *Journal of Volcanology and Geothermal Research* **202**, 153–166.

Holtz, F., Sato, H., Lewis, J., Behrens, H. & Nakada, S. (2005). Experimental petrology of the 1991-1995 Unzen dacite, Japan. Part I: Phase relations, phase composition and pre-eruptive conditions. *Journal of Petrology* **46**, 319–337.

Hornby, A. J., Kendrick, J. E., Lamb, O. D., Hirose, T., De Angelis, S., von Aulock, F. W., Umakoshi, K., Miwa, T., Henton De Angelis, S., Wadsworth, F. B., Hess, K.-U., Dingwell, D. B. & Lavallée, Y. (2015). Spine growth and seismogenic faulting at Mt. Unzen, Japan. *Journal of Geophysical Research: Solid Earth* **120**, 4034–4054.

Horwell, C., Williamson, B., Llewellin, E., Damby, D. & Blond, J. (2013). The nature and formation of cristobalite at the Soufrière Hills volcano, Montserrat: implications for the petrology and stability of silicic lava domes. *Bulletin of Volcanology* **75**, 1–19.

Hoshizumi, H., Uto, K. & Watanabe, K. (1999). Geology and Eruptive History of Unzen Volcano, Shimabara Peninsula, Kyushu, SW Japan. *Journal of Volcanology and Geothermal Research* **89**, 81–94.

Iverson, R. M. (2008). Dynamics of seismogenic volcanic extrusion resisted by a solid surface plug, Mount St. Helens, 2004-2005. In: Sherrod, D. R., Scott, W. E. & Stauffer, P. H. (eds.) *A Volcano Rekindled: The Renewed Eruption of Mount St. Helens, 2004-2006. Professional Paper 1750.*: U.S. Geological Survey 425–460.

Iverson, R. M., Dzurisin, D., Gardner, C. A., Gerlach, T. M., LaHusen, R. G., Lisowski, M., Major, J. J., Malone, S. D., Messerich, J. A., Moran, S. C., Pallister, J. S., Qamar, A. I., Schilling, S. P. & Vallance, J. W. (2006). Dynamics of seismogenic volcanic extrusion at Mount St Helens in 2004-05. *Nature* **444**, 439–443.

Johnson, J. B., Lyons, J. J., Andrews, B. J. & Lees, J. M. (2014). Explosive dome eruptions modulated by periodic gas-driven inflation. *Geophysical Research Letters* **41**, 6689–6697.

Kendrick, J. E., Lavallée, Y., Ferk, A., Perugini, D., Leonhardt, R. & Dingwell, D. B. (2012). Extreme frictional processes in the volcanic conduit of Mount St. Helens (USA) during the 2004–2008 eruption. *Journal of Structural Geology* **38**, 61–76.

Kendrick, J. E., Lavallée, Y., Hess, K. U., De Angelis, S., Ferk, A., Gaunt, H. E., Meredith, P. G., Dingwell, D. B. & Leonhardt, R. (2014a). Seismogenic frictional melting in the magmatic column. *Solid Earth* **5**, 199–208.

Kendrick, J. E., Lavallée, Y., Hess, K. U., Heap, M. J., Gaunt, H. E., Meredith, P. G. & Dingwell, D. B. (2013). Tracking the permeable porous network during strain-dependent magmatic flow. *Journal of Volcanology and Geothermal Research* **260**, 117–126.

Kendrick, J. E., Lavallée, Y., Hirose, T., Di Toro, G., Hornby, A., De Angelis, S. & Dingwell, D. B. (2014b). Volcanic drumbeat seismicity caused by stick-slip motion and magmatic frictional melting. *Nature Geoscience* **7**, 438–442.

Kendrick, J. E., Lavallée, Y., Mariani, E., Dingwell, D. B., Wheeler, J. & Varley, N. R. (2017). Crystal plasticity as an indicator of the viscous-brittle transition in magmas. *Nature Communications* **8**, 1926.

Kendrick, J. E., Lavallee, Y., Varley, N. R., Wadsworth, F. B., Lamb, O. D. & Vasseur, J. (2016). Blowing Off Steam: Tuffisite Formation As a Regulator for Lava Dome Eruptions. *Frontiers in Earth Science* **4**.

Kennedy, B. M., Jellinek, A. M., Russell, J. K., Nichols, A. R. L. & Vigouroux, N. (2010). Time-and temperature-dependent conduit wall porosity: A key control on degassing and explosivity at Tarawera volcano, New Zealand. *Earth and Planetary Science Letters* **299**, 126–137.

Kennedy, L. A., Russell, J. K. & Nelles, E. (2009). Origins of Mount St. Helens cataclasites: Experimental insights. *American Mineralogist* **94**, 995–1004.

Kohno, Y., Matsushima, T. & Shimizu, H. (2008). Pressure sources beneath Unzen Volcano inferred from leveling and GPS data. *Journal of Volcanology and Geothermal Research* **175**, 100–109.

Krása, D. & Herrero-Bervera, E. (2005). Alteration induced changes of magnetic fabric as exemplified by dykes of the Koolau volcanic range. *Earth and Planetary Science Letters* **240**, 445–453.

Kueppers, U., Scheu, B., Spieler, O. & Dingwell, D. B. (2005). Field-based density measurements as tool to identify preeruption dome structure: set-up and first results from Unzen volcano, Japan. *Journal of Volcanology and Geothermal Research* **141**, 65–75.

Lamb, O. D., De Angelis, S., Umakoshi, K., Hornby, A. J., Kendrick, J. E. & Lavallee, Y. (2015). Repetitive fracturing during spine extrusion at Unzen volcano, Japan. *Solid Earth* **6**, 1277–1293.

Lamur, A., Kendrick, J. E., Eggertsson, G. H., Wall, R. J., Ashworth, J. D. & Lavallee, Y. (2017). The permeability of fractured rocks in pressurised volcanic and geothermal systems. *Scientific Reports* **7**.

Laumonier, M., Arbaret, L., Burgisser, A. & Champallier, R. (2011). Porosity redistribution enhanced by strain localization in crystal-rich magmas. *Geology* **39**, 715–718.

Lavallée, Y., Benson, P. M., Heap, M. J., Hess, K. U., Flaws, A., Schillinger, B., Meredith, P. G. & Dingwell, D. B. (2013). Reconstructing magma failure and the degassing network of dome-building eruptions. *Geology* **41**, 515–518.

Lavallée, Y., Dingwell, D. B., Johnson, J. B., Cimarelli, C., Hornby, A. J., Kendrick, J. E., von Aulock, F. W., Kennedy, B. M., Andrews, B. J., Wadsworth, F. B., Rhodes, E. & Chigna, G. (2015). Thermal vesiculation during volcanic eruptions. *Nature* **528**, 544–547.

Lavallée, Y., Hess, K. U., Cordonnier, B. & Dingwell, D. B. (2007). Non-Newtonian rheological law for highly crystalline dome lavas. *Geology* **35**, 843–846.

Lavallée, Y., Meredith, P. G., Dingwell, D. B., Hess, K. U., Wassermann, J., Cordonnier, B., Gerik, A. & Kruhl, J. H. (2008). Seismogenic lavas and explosive eruption forecasting. *Nature* **453**, 507-510.

Lavallée, Y., Mitchell, T. M., Heap, M. J., Vasseur, J., Hess, K.-U., Hirose, T. & Dingwell, D. B. (2012a). Experimental generation of volcanic pseudotachylytes: Constraining rheology. *Journal of Structural Geology* **38**, 222–233.

Lavallée, Y., Varley, N., Alatorre-Ibargüengoitia, M., Hess, K. U., Kueppers, U., Mueller, S., Richard, D., Scheu, B., Spieler, O. & Dingwell, D. (2012b). Magmatic architecture of dome-building eruptions at Volcán de Colima, Mexico. *Bulletin of Volcanology* **74**, 249-260.

Lejeune, A. M. & Richet, P. (1995). Rheology of Crystal-Bearing Silicate Melts - An Experimental study at High Viscosities. *Journal of Geophysical Research* **100**, 4215–4229.

Lensky, N. G., Sparks, R. S. J., Navon, O. & Lyakhovsky, V. (2008). Cyclic activity at Soufrière Hills Volcano, Montserrat: degassing-induced pressurization and stick-slip extrusion. *Geological Society, London, Special Publications* **307**, 169–188.

Leonhardt, R. (2006). Analyzing rock magnetic measurements: The RockMagAnalyzer 1.0 software. *Computers & Geosciences* **32**, 1420–1431.

Llewellin, E. W. & Manga, M. (2004). Bubble suspension rheology and implications for conduit flow. *Journal of Volcanology and Geothermal Research* **143**, 205–217.

Mariani, E., Mecklenburgh, J., Wheeler, J., Prior, D. J. & Heidelbach, F. (2009). Microstructure evolution and recrystallization during creep of MgO single crystals. *Acta Materialia* **57**, 1886–1898.

Mason, R. M., Starostin, A. B., Melnik, O. E. & Sparks, R. S. J. (2006). From Vulcanian explosions to sustained explosive eruptions: The role of diffusive mass transfer in conduit flow dynamics. *Journal of Volcanology and Geothermal Research* **153**, 148–165.

Mastin, L. G. (2005). The controlling effect of viscous dissipation on magma flow in silicic conduits. *Journal of Volcanology and Geothermal Research* **143**, 17–28.

Melnik, O. & Sparks, R. S. J. (2002). Dynamics of magma ascent and lava extrusion at Soufrière Hills Volcano, Montserrat. *Geological Society, London, Memoirs* **21**, 153–171.

Michaut, C., Bercovici, D. & Sparks, R. S. J. (2009). Ascent and compaction of gas rich magma and the effects of hysteretic permeability. *Earth and Planetary Science Letters* **282**, 258–267.

Miyabuchi, Y. (1999). Deposits associated with the 1990-1995 eruption of Unzen volcano, Japan. *Journal of Volcanology and Geothermal Research* **89**, 139–158.

Monzawa, N. & Otsuki, K. (2003). Comminution and fluidization of granular fault materials: implications for fault slip behavior. *Tectonophysics* **367**, 127–143.

Morgavi, D., Perugini, D., De Campos, C. P., Ertel-Ingrisch, W. & Dingwell, D. B. (2013). Time evolution of chemical exchanges during mixing of rhyolitic and basaltic melts. *Contributions to Mineralogy and Petrology*
166, 615–638.

Moskowitz, B. M. (1981). Methods for Estimating Curie Temperatures of Titanomaghemites from Experimental Js-T Data. *Earth and Planetary Science Letters* **53**, 84–88.

Murphy, M. D., Sparks, R. S. J., Barclay, J., Carroll, M. R. & Brewer, T. S. (2000). Remobilization of andesite magma by intrusion of mafic magma at the Soufrière Hills Volcano, Montserrat, West Indies. *Journal of Petrology* **41**, 21–42.

Murray, J. D. (1979). Outlines of the structure and emplacement history of a tonalite plutons in the Peninsular Ranges batholith, northern Baja California, Mexico. In: Abbott, P. L. & Todd,

V. R. (eds.) *Mesozoic crystalline rocks: Peninsular ranges batholith and pegmatites, Point Sal Ophiolite*. San Diego State University, San Diego, California, 163–176.

Nakada, S. & Fujii, T. (1993). Preliminary-Report on the Activity at Unzen Volcano (Japan), November 1990 November 1991 - Dacite Lava Domes and Pyroclastic Flows. *Journal of Volcanology and Geothermal Research* **54**, 319–333.

Nakada, S., Miyake, Y., Sato, H., Oshima, O. & Fujinawa, A. (1995). Endogenous growth of dacitic dome at Unzen Volcano (Japan), 1993-1994. *Geology* **23**, 157–160.

Nakada, S. & Motomura, Y. (1999). Petrology of the 1991-1995 eruption at Unzen: effusion pulsation and groundmass crystallization. *Journal of Volcanology and Geothermal Research* **89**, 173–196.

Nakada, S., Shimizu, H. & Ohta, K. (1999). Overview of the 1990-1995 eruption at Unzen Volcano. *Journal of Volcanology and Geothermal Research* **89**, 1–22.

Nakamura, M. (1995). Continuous Mixing of Crystal Mush and Replenished Magma in the Ongoing Unzen Eruption. *Geology* **23**, 807–810.

Nakamura, N., Hirose, T. & Borradaile, G. J. (2002). Laboratory verification of submicron magnetite production in pseudotachylytes: relevance for paleointensity studies. . *Earth and Planetary Science Letters* **201**, 13–18.

Neuberg, J., Tuffen, H., Collier, L., Green, D., Powell, T. & Dingwell, D. (2006). The trigger mechanism of low-frequency earthquakes on Montserrat. *Journal of Volcanology and Geothermal Research* **153**, 37–50.

Noguchi, S., Toramaru, A. & Nakada, S. (2008a). Groundmass crystallization in dacite dykes taken in Unzen Scientific Drilling Project (USDP-4). *Journal of Volcanology and Geothermal Research* **175**, 71–81.

Noguchi, S., Toramaru, A. & Nakada, S. (2008b). Relation between microlite textures and discharge rate during the 1991-1995 eruptions at Unzen, Japan. *Journal of Volcanology and Geothermal Research* **175**, 141–155.

Ockendon, H. (2006). Channel flow with temperature-dependent viscosity and internal viscous dissipation. *Journal of Fluid Mechanics* **93**, 737–746.

Pallister, J. S., Cashman, K. V., Hagstrum, J. T., Beeler, N. M., Moran, S. C. & Denlinger, R. P. (2013). Faulting within the Mount St. Helens conduit and implications for volcanic earthquakes. *Geological Society of America Bulletin* **125**, 359–376.

Pallister, J. S., Thornber, C. R., Cashman, K. V., Clynne, M. A., Lowers, H. A., Mandeville, C. W., Brownfield, I. K. & Meeker, G. P. (2008). Petrology of the 2004-2006 Mount St Helens lava dome - implications for magmatic plumbing and eruption triggering. In: Sherrod, D. R., Scott, W. E. & Stauffer, P. H. (eds.) *A Volcano Rekindled: The Renewed Eruption of Mount St. Helens, 2004-2006. Professional Paper 1750.*: U.S. Geological Survey, 647–703.

Perugini, D. & Poli, G. (2012). The mixing of magmas in plutonic and volcanic environments: Analogies and differences. *Lithos* **153**, 261–277.

Picard, D., Arbaret, L., Pichavant, M., Champallier, R. & Launeau, P. (2011). Rheology and microstructure of experimentally deformed plagioclase suspensions. *Geology* **39**, 747–750.

Pirrie, D., Butcher, A. R., Power, M. R., Gottlieb, P. & Miller, G. L. (2004). Rapid quantitative mineral and phase analysis using automated scanning electron microscopy (QEMSCAN®);

potential applications in forensic geoscience. In: Pye, K. & Croft, D. J. (eds.) *Forensic Geoscience, Principles, Techniques and Applications*. London: Geological Society Special Publication, 23–136.

Plechov, P. Y., Tsai, A. E., Shcherbakov, V. D. & Dirksen, O. V. (2011). Opacitization conditions of hornblende in Bezymyannyi volcano andesites (March 30, 1956 eruption). *Petrology* **16**, 19–35.

Poirier, J. P. (1995). Plastic rheology of crystals. *Mineral Physics & Crystallography: A Handbook of Physical Constants*. Washington, DC: AGU, 237–247.

Prior, D. J., Boyle, A. P., Brenker, F., Cheadle, M. C., Day, A., Lopez, G., Peruzzo, L., Potts, G. J., Reddy, S., Spiess, R., Timms, N. E., Trimby, P., Wheeler, J. & Zetterstrom, L. (1999). The application of electron backscatter diffraction and orientation contrast imaging in the SEM to textural problems in rocks. *American Mineralogist* **84**, 1741–1759.

Prior, D. J., Mariani, E. & Wheeler, J. (2009). EBSD in the earth sciences: applications, common practice, and challenges. In: Schwartz, A. J., Kumar, M., Adams, B. L. & Field, D. P. (eds.) *Electron Backscatter Diffraction in Materials Science*. New York: Springer Science, 345–360.

Rosi, M., Landi, P., Polacci, M., Di Muro, A. & Zandomeneghi, D. (2004). Role of conduit shear on ascent of the crystal-rich magma feeding the 800-year-BP Plinian eruption of Quilotoa Volcano (Ecuador). *Bulletin of Volcanology* **66**, 307–321.

Rutherford, M. J. & Devine, J. D. (2003). Magmatic conditions and magma ascent as indicated by hornblende phase equilibria and reactions in the 1995-2002 Soufriere Hills magma. *Journal of Petrology* **44**, 1433–1454.

Rutherford, M. J. & Hill, P. M. (1993). Magma Ascent Rates from Amphibole Breakdown - an Experimental-Study Applied to the 1980-1986 Mount St-Helens Eruptions. *Journal of Geophysical Research: Solid Earth* **98**, 19667–19685.

Ryan, A. G., Friedlander, E. A., Russell, J. K., Heap, M. J. & Kennedy, L. A. (2018). Hot pressing in conduit faults during lava dome extrusion: Insights from Mount St. Helens 2004-2008. *Earth and Planetary Science Letters* **482**, 171–180.

Saito, T., Ishikawa, N. & Kamata, H. (2007). Magnetic petrology of the 1991-1995 dacite lava of Unzen volcano, Japan: Degree of oxidation and implications for the growth of lava domes. *Journal of Volcanology and Geothermal Research* **164**, 268–283.

Saito, T. & Shikawa, N. (2007). Magnetic petrology and its implication for magma mixing of the 1991-1995 dacite at Unzen volcano, Japan. *Earth Planets and Space* **59**, 863–870.

Sakuma, S., Kajiwara, T., Nakada, S., Uto, K. & Shimizu, H. (2008). Drilling and logging results of USDP-4 - Penetration into the volcanic conduit of Unzen Volcano, Japan. *Journal of Volcanology and Geothermal Research* **175**, 1–12.

Salaun, A., Villemant, B., Gerard, M., Komorowski, J. C. & Michel, A. (2011). Hydrothermal alteration in andesitic volcanoes: Trace element redistribution in active and ancient hydrothermal systems of Guadeloupe (Lesser Antilles). *Journal of Geochemical Exploration* **111**, 59–83.

Sato, H., Fujii, T. & Nakada, S. (1992). Crumbling of Dacite Dome Lava and Generation of Pyroclastic Flows at Unzen Volcano. *Nature* **360**, 664–666.

Sato, H., Holtz, F., Botcharnikov, R. E. & Nakada, S. (2017). Intermittent generation of mafic enclaves in the 1991-1995 dacite of Unzen Volcano recorded in mineral chemistry. *Contributions to Mineralogy and Petrology* **172**, 22.

Sato, H., Nakada, S., Fujii, T., Nakamura, M. & Suzuki-Kamata, K. (1999). Groundmass pargasite in the 1991-1995 dacite of Unzen volcano: phase stability experiments and volcanological implications. *Journal of Volcanology and Geothermal Research* **89**, 197–212.

Schneider, C. A., Rasband, W. S. & Eliceiri, K. W. (2012). NIH Image to ImageJ: 25 years of image analysis. *Nature Methods* **9**, 671–675.

Scott, J. A. J., Mather, T. A., Pyle, D. M., Rose, W. I. & Chigna, G. (2012). The magmatic plumbing system beneath Santiaguito Volcano, Guatemala. *Journal of Volcanology and Geothermal Research* **237**, 54–68.

Selverstone, J., Axen, G. J. & Luther, A. (2012). Fault localization controlled by fluid infiltration into mylonites: Formation and strength of low-angle normal faults in the midcrustal brittle-plastic transition. *Journal of Geophysical Research: Solid Earth* **117**.

Shimamoto, T. & Tsutsumi, A. (1994). A new rotary-shear high-speed frictional testing machine: its basic design and scope of research. *Structural Geology: Journal of the Tectonic Research Group of Japan* **39**, 65–78.

Smith, J. V., Miyake, Y. & Oikawa, T. (2001). Interpretation of porosity in dacite lava domes as ductile-brittle failure textures. *Journal of Volcanology and Geothermal Research* **112**, 25–35.

Sparks, R. S. J. (1997). Causes and consequences of pressurisation in lava dome eruptions. *Earth and Planetary Science Letters* **150**, 177–189.

Tanaka, H. K. M. (2016). Instant snapshot of the internal structure of Unzen lava dome, Japan with airborne muography. *Scientific Reports* **6**.

Tanguy, J. C. (2004). Rapid dome growth at Montagne Pelee during the early stages of the 1902-1905 eruption: a reconstruction from Lacroix's data. *Bulletin of Volcanology* **66**, 615–621.

Tuffen, H. & Dingwell, D. (2005). Fault textures in volcanic conduits: evidence for seismic trigger mechanisms during silicic eruptions. *Bulletin of Volcanology* **67**, 370–387.

Tuffen, H., Dingwell, D. B. & Pinkerton, H. (2003). Repeated fracture and healing of silicic magma generate flow banding and earthquakes? *Geology* **31**, 1089–1092.

Tuffen, H., James, M. R., Castro, J. & Schipper, C. I. (2013). Exceptional mobility of an advancing rhyolitic obsidian flow at Cordón Caulle volcano in Chile. *Nature Communications* **4**, 2709.

Ui, T., Matsuwo, N., Sumita, M. & Fujinawa, A. (1999). Generation of block and ash flows during the 1990-1995 eruption of Unzen Volcano, Japan. *Journal of Volcanology and Geothermal Research* **89**, 123–137.

Umakoshi, K., Shimizu, H. & Matsuwo, N. (2001). Volcano-tectonic seismicity at Unzen Volcano, Japan 1985-1999. *Journal of Volcanology and Geothermal Research* **112**, 117–131.

Umakoshi, K., Takamura, N., Shinzato, N., Uchida, K., Matsuwo, N. & Shimizu, H. (2008). Seismicity associated with the 1991-1995 dome growth at Unzen Volcano, Japan. *Journal of Volcanology and Geothermal Research* **175**, 91–99.

Vedeneeva, E. A., Melnik, O. E., Barmin, A. A. & Sparks, R. S. J. (2005). Viscous dissipation in explosive volcanic flows. *Geophysical Research Letters* **32**.

Venezky, D. Y. & Rutherford, M. J. (1999). Petrology and Fe-Ti oxide reequilibration of the 1991 Mount Unzen mixed magma. *Journal of Volcanology and Geothermal Research* **89**, 213–230.

Vernon, R. H. (2000). Review of Microstructural Evidence of Magmatic and Solid-State Flow. *Visual Geosciences* **5**, 1–23.

Vernon, R. H. & Paterson, S. R. (1993). The Ardara Pluton, Ireland - Deflating All Expanded Intrusion. *Lithos* **31**, 17–32.

Voight, B., Sparks, R. S., Miller, A. D., Stewart, R. C., Hoblitt, R. P., Clarke, A., Ewart, J., Aspinall, W. P., Baptie, B., Calder, E. S., Cole, P., Druitt, T. H., Hartford, C., Herd, R. A., Jackson, P., Lejeune, A. M., Lockhart, A. B., Loughlin, S. C., Luckett, R., Lynch, L., Norton, G. E., Robertson, R., Watson, I. M., Watts, R. & Young, S. R. (1999). Magma Flow Instability and Cyclic Activity at Soufriere Hills Volcano, Montserrat, British West Indies. *Science* **283**, 1138–1142.

Webb, S. L. & Dingwell, D. B. (1990). Non-Newtonian rheology of igneous melts at high stresses and strain rates: experimental results for rhyolite, andesite, basalt and nephelinite. *Journal of Geophysical Research* **95**, 15695–15701.

Wibberley, C. (1999). Are feldspar-to-mica reactions necessarily reaction-softening processes in fault zones? *Journal of Structural Geology* **21**, 1219–1227.

Wohlfarth, E. P. (1958). Relations between different modes of acquisition of the remanent magnetization of ferromagnetic particles. *Journal of Applied Physics* **29**, 595–596.

Wright, H. M. N. & Weinberg, R. F. (2009). Strain localization in vesicular magma: Implications for rheology and fragmentation. *Geology* **37**, 1023–1026.

Yamamoto, T., Takarada, S. & Suto, S. (1993). Pyroclastic Flows from the 1991 Eruption of Unzen Volcano, Japan. *Bulletin of Volcanology* **55**, 166–175.

Yamashina, K., Matsushima, T. & Ohmi, S. (1999). Volcanic deformation at Unzen, Japan, visualized by a time-differential stereoscopy. *Journal of Volcanology and Geothermal Research* **89**, 73–80.

Yonkee, W. A., Czeck, D. M., Nachbor, A. C., Barszewski, C., Pantone, S., Balgord, E. A. & Johnson, K. R. (2013). Strain accumulation and fluid-rock interaction in a naturally deformed diamictite, Willard thrust system, Utah (USA): Implications for crustal rheology and strain softening. *Journal of Structural Geology* **50**, 91–118.

Zibra, I., Kruhl, J. H., Montanini, A. & Tribuzio, R. (2012). Shearing of magma along a high-grade shear zone: Evolution of microstructures during the transition from magmatic to solid-state flow. *Journal of Structural Geology* **37**, 150–160.

FIGURE CAPTIONS

Fig. 1. Unzen volcano and lava dome heterogeneity. (a) Map showing the location of Unzen volcano in southwestern Japan (source: Esri, DeLorme Publishing Company, Inc.). The inset shows the Shimabara Peninsula with Unzen volcano denoted with a triangle. (b) View of the eastern side of the Unzen lava dome. (c) Dome summit displaying large, polygonal blocks with a range of deformation textures and variable degrees of oxidation. The lava spine can be seen having extruded from the top of the dome. (d) Eastern side of the 1994–1995 lava spine revealing multiple, broken segments and larger *in situ* slabs, with the main spine residing in

the background. (e) Example of an undeformed dome block with no macroscopic deformation, little alteration and negligible oxidation. (f) Close up textures of an undeformed block consisting of large, euhedral, white plagioclase phenocrysts, along with dark amphibole and biotite crystals. (g) Example of a highly-deformed dome block with moderate oxidation, consisting of shear bands and conjugate fractures. (h) Close-up textures of an extremely deformed block consisting of smeared plagioclase phenocrysts and elongated, oxidised amphibole crystals.

Fig. 2. Field and textural observations of the outcrop 1 marginal shear zone of the Unzen lava spine. (a) Photograph of the shear zone, which has been separated into four zones according to style and intensity of deformation, along with sample collection locations (points A–H). On the surface of the high shear zone, principle shear lineations (PS), and Riedel shear textures (R and R') are visible, consistent with an upward movement of the spine. In panels (b–j), the left-hand side is the outcrop surface and the right-hand side is the corresponding plane polarised light photomicrograph. (b) Gouge, a well-consolidated, reddish gouge layer consisting of cataclastic deformation textures in the form of abundant crystal fragments, larger intact clasts and surface fractures. (c–e) High shear zone, displaying strong lineations and elongated white filaments that decrease in intensity from (c) to (e). Photomicrographs in (c) and (d) show that these filaments are comprised of plagioclase phenocryst fragments, with the elongated yellow-green dye representing voids where some fragments were removed. Fragments of amphibole are also observed within the groundmass. (f–g) Moderate shear zone: individual crystals are more visible, representing larger fragments, and elongated filaments of plagioclase crystals are less apparent. Lineations are less intense, although still visible on the outcrop surface. (h–i) Low shear zone, a smooth outcrop surface with negligible deformation, consisting of intact, euhedral plagioclase and amphibole phenocrysts. (j) Undeformed dome

block, consisting of large, euhedral plagioclase and amphibole phenocrysts, closely resembling the low shear zone.

Fig. 3. Photograph of the outcrop 2 shear zone used for the investigation of magnetic properties of the Unzen lava spine. (a) The shear zone is an end-on exposure of the eastern section of the spine, subdivided into four discrete units (host, high shear zone, gouge and breccia), as described by Hornby *et al.* (2015). The outlined areas (T1 and T2) are the locations of two transects across the shear zone margin where field magnetic measurements were taken. In panels (b–d), the left-hand side is the outcrop surface and the right-hand side is the corresponding plane polarised light photomicrograph. (b) The host material represents the undeformed interior of the spine, akin to the low shear zone of outcrop 1. (c) High shear zone, consisting of elongated, white filaments similar to those observed in outcrop 1 and fragments of broken crystals. (d) A red, cataclastic gouge layer (~0.6 m wide) situated between the high shear zone and breccia, dominated by finely comminuted crystals.

Fig. 4. QEMSCAN mineral distribution maps of the gouge, high shear, moderate shear and low shear zones from outcrop 1. Top row panels are whole thin section scans taken in plane polarised light (PPL), followed by QEMSCAN maps with all phases highlighted and each colour representing a different mineral or glass phase (pore space in white). The bottom five rows are maps of each phase isolated, providing a clearer assessment of the variations across the shear zone and allowing a quantitative comparison of their modality (see Table 2). Arrows denote the extrusion direction. Note: Si polymorphs represent all SiO_2 phases, including quartz phenocrysts and groundmass cristobalite.

Fig. 5. Groundmass mineralogy, glass and porosity textures of the gouge, high shear and low shear zones using QEMSCAN. Plagioclase microlites are equant and tabular; they are randomly orientated in the low shear zone and preferentially aligned in the extrusion direction in the high shear zone, while the gouge consists of angular fragments derived from broken phenocrysts. Groundmass amphibole (pargasite) is present in all three zones as ellipsoidal microlites, with occasional hollow cores. Si polymorphs in the groundmass of the low shear and high shear zone are discrete, isolated crystals often filling or surrounding pores, while in the gouge these are smaller and localised within the interstitial glass. These inherent differences are reflected in the glass variation, with the gouge being glass-poor relative to the high and low shear zones. Pores in the low shear zone are abundant and irregular shaped, often connected to form a permeable pathway, whereas the high shear pores are smaller, less abundant and typically isolated with no connectivity. The pores within the gouge sit intermediate between the low and high shear zone.

Fig. 6. Photomicrographs in plane polarised light of comparative groundmass flow textures from high, moderate and low shear zones. (a) Tabular microlites and microphenocrysts of plagioclase (Pl) and amphibole (amp) in the high shear zone have a strong preferential alignment in the extrusion direction, localising as flow bands that envelope larger crystal fragments resulting in pressure shadows (PS) at the tips of the crystal fragment. (b) The moderate shear zone has only minor alignment of tabular crystals, while the low shear zone (c) displays a random orientation of tabular crystals. Pores (yellow-green dye) are also systematically smaller in size and lower in abundance from the low shear to high shear zone.

Fig. 7. Crystal size and shape distribution of plagioclase phenocrysts across the shear zone. (a) Plane polarised light thin section scans of each sample (A–H) across the shear zone and

binary images of plagioclase phenocrysts (>0.01 mm^2) used for quantification. Each sample represents between 150–550 crystals depending on the number of phenocrysts present. Plagioclase phenocrysts size variation (b) and circularity variation (c) are shown with distance from the gouge. Both box plots show 25^{th} and 75^{th} percentile, the median value and whiskers outlining the 1–99% range. Diamonds represent outliers within the dataset and squares are the mean value per sample connected by the dashed line. Errors were calculated from repeat thresholding of the crystals and re-analysis.

Fig. 8. Plastic deformation of plagioclase and biotite phenocrysts measured by electron backscatter diffraction (EBSD). For each panel (a–c), the left-hand side shows a plane polarised light photomicrograph of the crystal analysed and on the right-hand side is the corresponding band-contrast misorientation map. Colours represent the amount of misorientation relative to a selected point along the crystal, with an angular resolution of ± 0.5º. All points were chosen at one end of the crystal in order to observe the maximum misorientation along the crystal's major axis and are labelled in (a–c) with a white circle and cross. (a) Three fractured segments of a single plagioclase phenocryst from the gouge (Fig. 2b) displaying negligible internal deformation across each. Unlike plagioclase, biotite phenocrysts display extensive plastic deformation throughout the high shear zone. (b) A plastically deformed biotite crystal from the high shear zone (Fig. 2d), revealing a partial tear upon reaching its plastic limit in areas of highest lattice distortion. (c) A biotite phenocryst that deformed plastically in the high shear zone (Fig. 2d), producing an S-C style fabric, and ruptured along a shear band parallel to the extrusion direction, forming fragments with variable plasticity.

Fig. 9. Plastic deformation of plagioclase microlites across the shear zone. (a) Greyscale band contrast maps with plagioclase microlites subjected to a texture component analysis. The colour gradient displays the relative misorientation across a single microlite grain, thresholding to display up to 8º lattice distortion, and visualised by drawing misorientation transects along the crystals' axis from blue to red (T1 and T2). All misorientation angles have resolution error of ± 0.5º. The dashed outlined areas in the gouge indicate crystalline silica phases owing to glass alteration. (b) Normalised frequency histogram of crystal plastic distortion from each section of the shear zone, binned every 1º misorientation. (c) Box plot of the intensity of plastic deformation represented by the misorientation per micron. The box highlights the 25th and 75th percentiles (the bottom and top of the boxes, respectively) and the whiskers show the data range. The horizontal line in the box marks the median value and the square represents the mean for each section of the shear zone. (d) Maximum misorientation within a single plagioclase microlite versus its length. The gradients of the lines represent the modelled degree of crystal lattice distortion for a given crystal length in each section of the shear zone. These misorientation gradients were modelled by multiplying the mean misorientation per micron, as shown in (c), by an infinite crystal length. Plagioclase microlites in the undeformed dome block were also analysed for comparison.

Fig. 10. Field and laboratory magnetic susceptibility measurements. (a, b) Magnetic susceptibility across two different transects of the spine margin at outcrop 2 (T1 and T2 in Fig. 3a), measured using a Bartington portable magnetic susceptibility meter. The undeformed host rock (left in both panels) has the highest susceptibility, gradually decreasing through the highly sheared area to the lowest values in the red gouge layer and finally slightly higher values in the fault breccia on the right of the gouge. (c) Box plot of field magnetic susceptibility measurements of pristine and sheared loose dome rocks, which show values that

are comparable to transects in (a) and (b). These are compared to laboratory magnetic susceptibility measurements (marked grey zones; measured using a VFTB) on the host rock, highly sheared coherent lava and gouge. (d) Temperature-dependent bulk susceptibility during heating and cooling cycles (measured using a Kappabridge) for the three rock types. Susceptibility is highest in the host, intermediate in the highly-sheared zone and lowest in the gouge and the magneto-mineralogy and stability are distinguishable. (e) Comparison of the ratio of saturation remanence and saturation magnetisation (M_{rs}/M_s) to the coercive force (B_c), showing that the gouge has significantly different remanence carriers. (f) Day plot combining hysteresis and backfield data showing each section of the shear zone has discrete differences. (g) M_{rs}/M_s *versus* the coercivity ratio (B_{rh}/B_{cr}) reinforces the disparate evolution of the high shear and gouge from the host lava.

Fig. 11. (a) Backscatter electron (BSE) images of the groundmass textures across the shear zone showing the progressive alteration of the groundmass glass and variations in pargasite reactions rims, both compared to the undeformed dome block. In the low shear zone and undeformed dome block, clusters of small, dark grey silica-rich patches are located around microlites. These clusters in the moderate shear zone spread into web-like domains that increase in abundance in the high shear zone. The gouge is texturally distinct from the rest of the shear zone, consisting of larger silica-rich patches that are well distributed within the groundmass. Pargasite crystals are surrounded by granular rims in the gouge material, both granular and symplectitic rims in the high shear zone, and symplectitic rims only in the moderate and low shear zones, with the undeformed dome block showing negligible reaction rims. (b) Box plot showing the maximum thickness of pargasite reaction rims for >30 crystals measured per section of the shear zone. The plot shows the 25th and 75th percentiles, data range, median value (horizontal line) and mean value (square). Thickness error was calculated

from the pixel resolution of the BSE images. Pargasite rim thicknesses show an average increase towards the gouge.

Fig. 12. Composition of the interstitial glass across the shear zone. (a) SiO_2 and TiO_2. (b) Al_2O_3 and K_2O. (c) Na_2O and CaO. (d) FeO and MgO. All values are presented on a volatile-free basis, with totals normalised to 100 wt %. Error bars adjacent to the corresponding component axis denote the relative uncertainty based on repeat analyses of KN-18 glass standard.

Fig. 13. High-temperature, high-velocity rotary shear (HVR) experiment and associated textures of the experimental shear zone. (a) Temperature evolution across a 2 mm transect of the slip zone through time derived from the thermographic recording of the experimental slip zone (b). The dashed line in (a) denotes the calorimetric glass transition (790 ºC) equating to a viscosity of 10^{12} Pa.s. (b) After ~10 seconds of slip, shear bands are observed radiating from the slip zone. The line across the slip zone in the thermographic images represents the location of the transect used to obtain the temperature profile in (a). Textural observations in (c), (d) and (e) can be directly compared to the temperature profile above. (c) QEMSCAN map and (d) photomicrograph showing the remobilisation of crystals and their alignment adjacent to the melt zone. (e) Porosity distribution showing that pores within the shear zone progressively decrease in size and abundance towards the slip plane. (f) BSE image of the experimental shear zone, being divided into four zones similar to the outcrop 1 shear zone, along with temperature estimates for each zone using the temperature profile in (a). Pargasites (Pg) in the experimental shear zone display pyroxene (Px) reaction rims in the areas of elevated temperature, being granular at the highest temperatures (g) and becoming finer further away (h). (i) Example of a pargasite crystal in the starting material displaying no

reaction rim. (j) A pargasite crystal from the gouge displaying a granular rim comparable to (g).

Fig. 14. A conceptual model of the shallow conduit at Unzen volcano prior to the extrusion of the 1994–1995 lava spine. Panels 1–4 represent the textural evolution of plagioclase, pargasite, biotite and pores (bubbles) during magma evolution to the surface. The colour gradient across the transects of the conduit represents a temperature profile derived from the rotary shear experiment. During magma ascent (1), an increase in crystallisation and volatile exsolution causes the flow to transition from a Poiseuille flow regime to a plug style ascent. An increase in viscosity of the crystal-rich magma permits strain to localise near the conduit margins causing deformation and formation of shear zones (2). Here, the increase in stress is manifested in the form of crystal rotation and alignment at the conduit margins. A thermal input likely accompanies viscous deformation due to shear heating, which causes a localised higher-temperature region towards the conduit margins resulting in the destabilisation of pargasite in the form of granular breakdown rims and pore compaction. As magma ascends further (3), it encounters the viscous-brittle transition, where biotite phenocrysts and plagioclase microlites can accommodate strain by deforming plastically, with crystal plasticity increasing towards the conduit margin. With further ascent, magma enters the brittle regime (4) causing strain localisation to be expressed by crystal comminution, which increases towards the conduit margins, where stress and strain are highest. The onset of brittle failure is accompanied by characteristic seismicity, as recorded during the extrusion of many domes and lava spines, where frictional behaviour takes over along the conduit margins. The slow extrusion of the high-temperature viscous spine is envisaged to experience late-stage oxidation, resulting in the formation of symplectitic pargasite breakdown rims accompanied with glass devitrification.

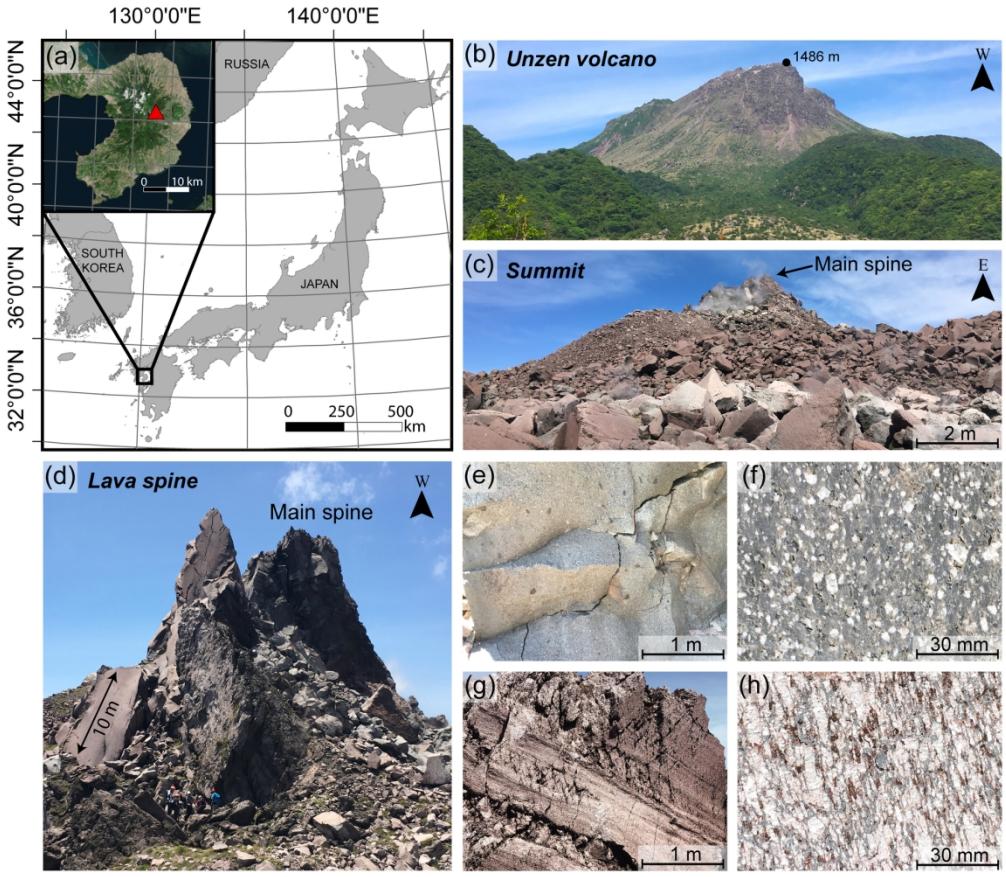

Fig. 1. Unzen volcano and lava dome heterogeneity. (a) Map showing the location of Unzen volcano in southwestern Japan (source: Esri, DeLorme Publishing Company, Inc.). The inset shows the Shimabara Peninsula with Unzen volcano denoted with a triangle. (b) View of the eastern side of Unzen lava dome. (c) Dome summit displaying large, polygonal blocks with a range of deformation textures and variable degrees of oxidation. The lava spine can be seen having extruded from the top of the dome. (d) Eastern side of the 1994–1995 lava spine revealing multiple, broken segments and larger in situ slabs, with the main spine residing in the background. (e) Example of an undeformed dome block with no macroscopic deformation, little alteration and negligible oxidation. (f) Close up textures of an undeformed block consisting of large, euhedral, white plagioclase phenocrysts, along with dark amphibole and biotite crystals. (g) Example of a highly deformed dome block with moderate oxidation, consisting of shear bands and conjugate fractures. (h) Close up textures of an extremely deformed block consisting of smeared plagioclase phenocrysts and elongated, oxidised amphibole crystals.

165x143mm (300 x 300 DPI)

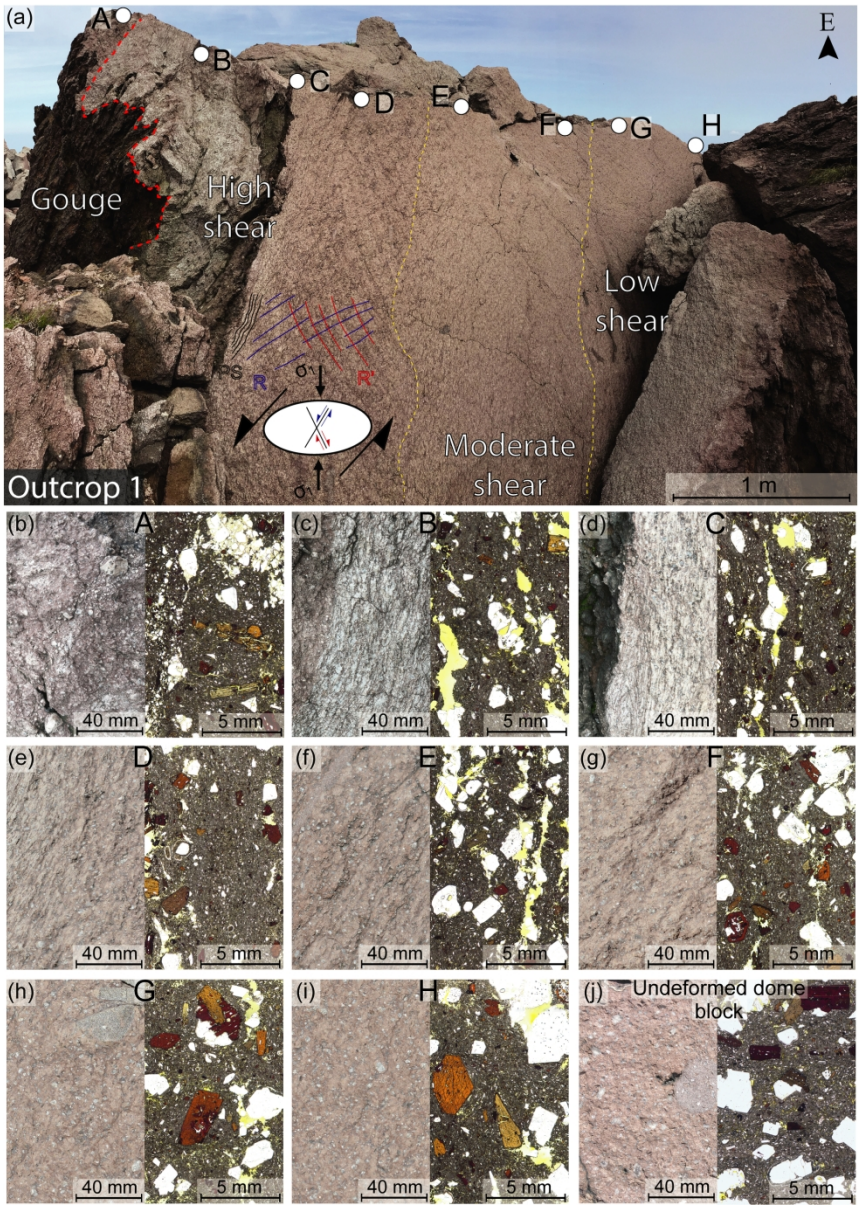

Fig. 2. Field and textural observations of outcrop 1 marginal shear zone of Unzen lava spine. (a) Photograph of the shear zone, which has been separated into four zones according to style and intensity of deformation, along with sample collection locations (points A–H). On the surface of the high shear zone, principle shear lineations (PS), and Riedel shear textures (R and R') are visible, consistent with an upward movement of the spine. In panels (b–j), the left-hand side is the outcrop surface and the right-hand side is the corresponding plane polarised light photomicrograph. (b) Gouge, a well-consolidated, reddish gouge layer consisting of cataclastic deformation textures in the form of abundant crystal fragments, larger intact clasts and surface fractures. (c–e) High shear zone, displaying strong lineations and elongated white filaments that decrease in intensity from (c) to (e). Photomicrographs in (c) and (d) show these filaments are comprised of plagioclase phenocryst fragments, with the elongated yellow-green dye representing voids where some fragments were removed. Fragments of amphibole are also observed within the groundmass. (f–g) Moderate shear zone, individual crystals are more visible, representing larger fragments, and elongated filaments of plagioclase crystals are less apparent. Lineations are less intense, although still visible on the outcrop surface. (h–i) Low shear zone, a smooth outcrop surface with negligible deformation, consisting of intact, euhedral plagioclase

and amphibole phenocrysts. (j) Undeformed dome block, consisting of large, euhedral plagioclase and amphibole phenocrysts, closely resembling the low shear zone.

165x231mm (300 x 300 DPI)

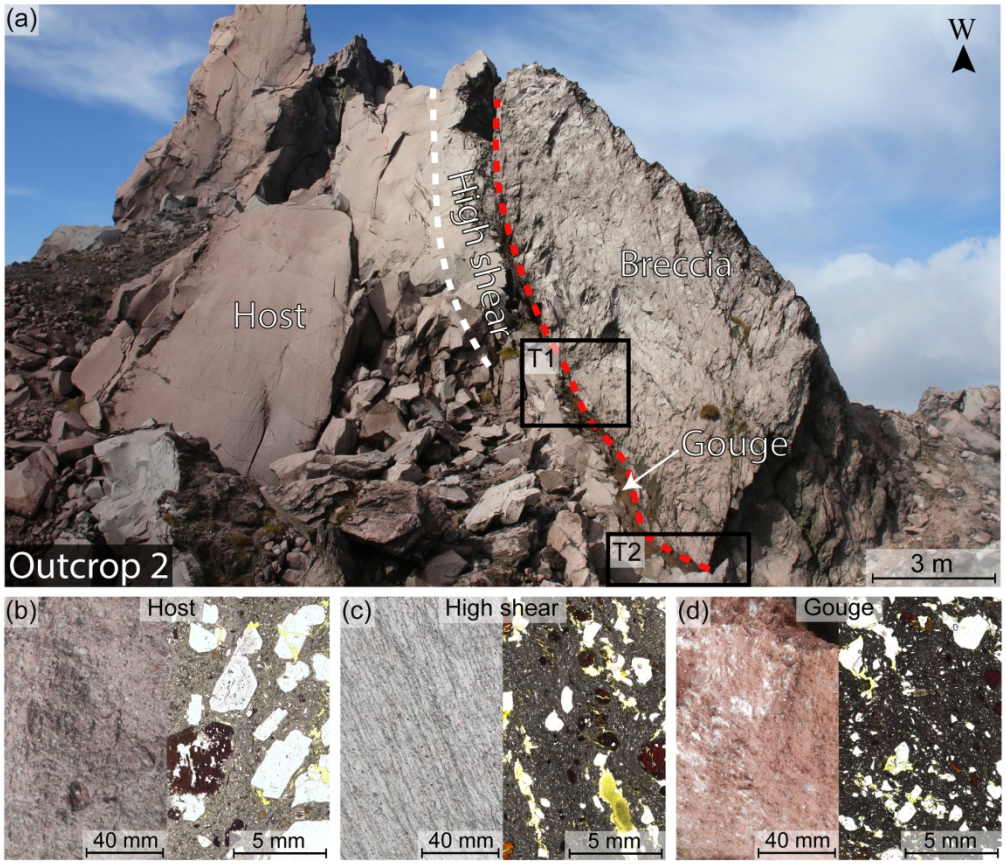

Fig. 3. Photograph of outcrop 2 shear zone used for the investigation of magnetic properties of Unzen lava spine. (a) The shear zone is an end-on exposure of the eastern section of the spine, subdivided into four discrete units (host, high shear zone, gouge and breccia), as described by Hornby *et al*. (2015). The outlined areas (T1 and T2) are the locations of two transects across the shear zone margin where field magnetic measurements were taken. In panels (b–d), the left-hand side is the outcrop surface and the right-hand side is the corresponding plane polarised light photomicrograph. (b) The host material represents an undeformed interior of the spine, akin to the low shear zone of outcrop 1. (c) High shear zone, consisting of elongated, white filaments similar to those observed in outcrop 1 and fragments of broken crystals. (d) A red, cataclastic gouge layer (~0.6 m wide) situated between the high shear zone and breccia, dominated by finely comminuted crystals.

164x141mm (300 x 300 DPI)

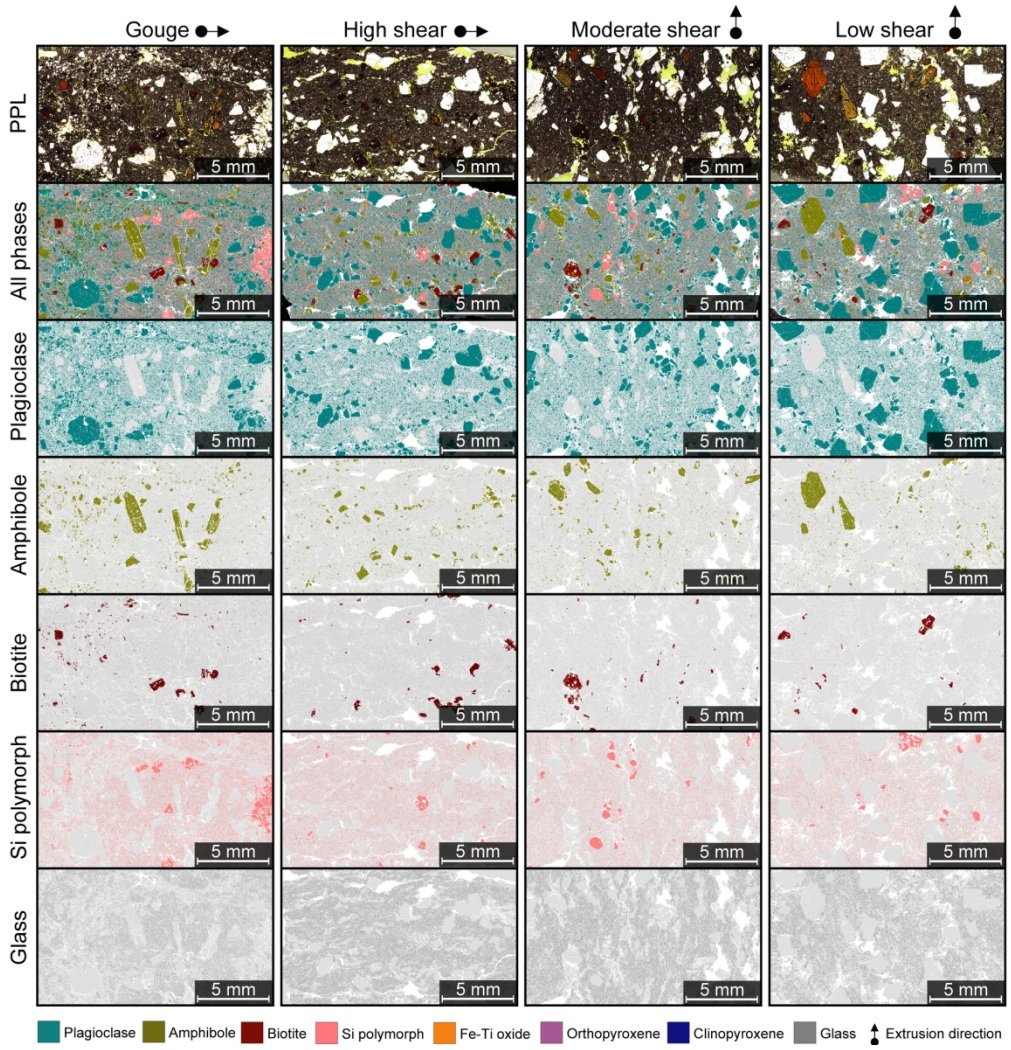

Fig. 4. QEMSCAN mineral distribution maps of the gouge, high shear, moderate shear and low shear zones from outcrop 1. Top row panels are whole thin section scans taken in plane polarised light (PPL), followed by QEMSCAN maps with all phases highlighted and each colour representing a different mineral or glass phase (pore space in white). The bottom five rows are maps of each phase isolated providing a clearer assessment of the variations across the shear zone and allowing a quantitative comparison of their modality (see Table 2). Arrows denote the extrusion direction. Note: Si polymorphs represent all SiO_2 phases, including quartz phenocrysts and groundmass cristobalite.

165x171mm (300 x 300 DPI)

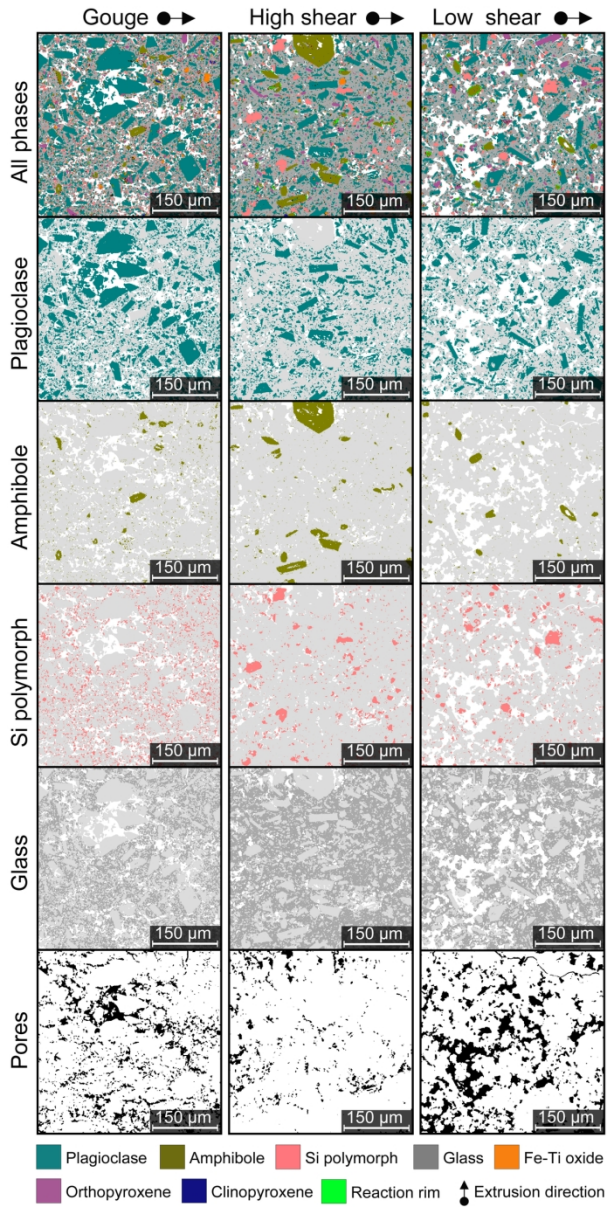

Fig. 5. Groundmass mineralogy, glass and porosity textures of the gouge, high shear and low shear zones using QEMSCAN. Plagioclase microlites are equant and tabular; they are randomly orientated in the low shear zone and preferentially aligned in the extrusion direction in the high shear zone, while the gouge consists of angular fragments derived from broken phenocrysts. Groundmass amphibole (pargasite) is present in all three zones as ellipsoidal microlites, with occasional hollow cores. Si polymorphs in the groundmass of the low shear and high shear zone are discrete, isolated crystals often filling or surround pores, while in the gouge these are smaller and localised within the interstitial glass. These inherent differences are reflected in the glass variation, with the gouge being glass-poor relative to the high and low shear zones. Pores in the low shear zone are abundant and irregular shaped, often connected to form a permeable pathway, whereas the high shear pores are smaller, less abundant and typically isolated with no connectivity. The pores within the gouge sit intermediate between the low and high shear zone.

104x209mm (300 x 300 DPI)

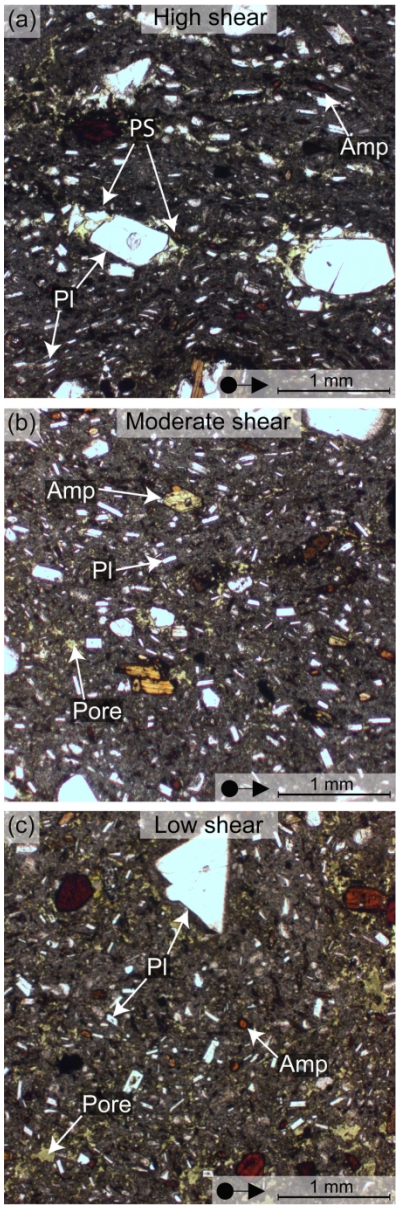

Fig. 6. Photomicrographs in plane polarised light of comparative groundmass flow textures from high, moderate and low shear zones. (a) Tabular microlites and microphenocrysts of plagioclase (Pl) and amphibole (amp) in the high shear zone have a strong preferential alignment in the extrusion direction, localising as flow bands that envelope larger crystal fragments resulting in pressure shadows (PS) at the tips of the crystal fragment. (b) The moderate shear zone has only minor alignment of tabular crystals, while the low shear zone (c) displays a random orientation of tabular crystals. Pores (yellow-green dye) are also systematically smaller in size and lower in abundance from the low shear to high shear zone.

70x214mm (300 x 300 DPI)

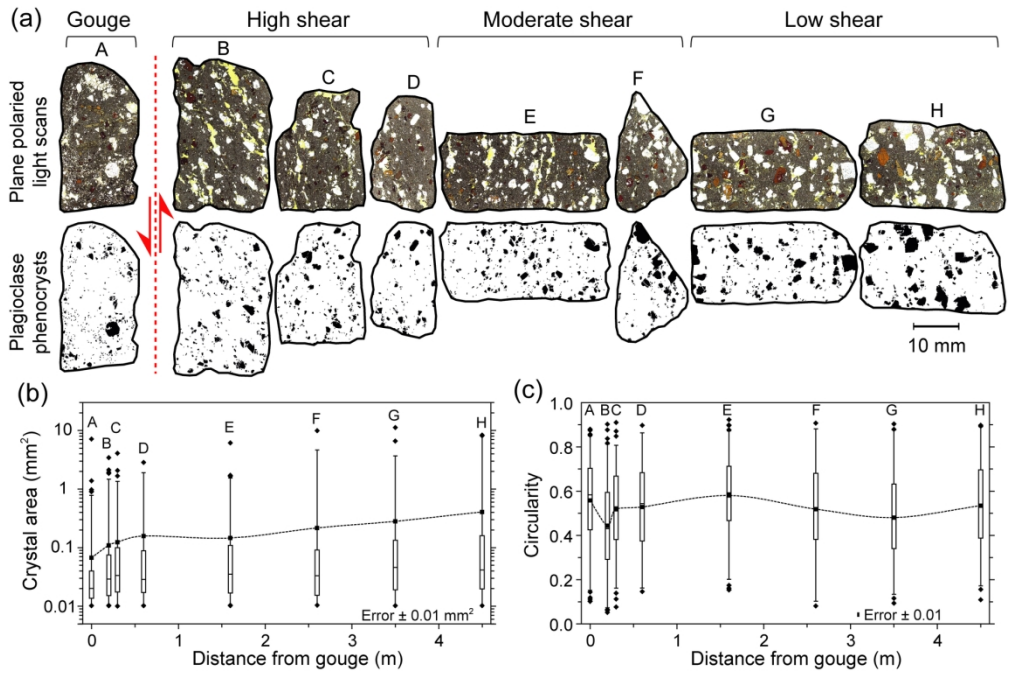

Fig. 7. Crystal size and shape distribution of plagioclase phenocrysts across the shear zone. (a) Plane polarised light thin section scans of each sample (A–H) across the shear zone and binary images of plagioclase phenocrysts (>0.01 mm^2) used for quantification. Each sample represents between 150–550 crystals depending on the number of phenocrysts present. Plagioclase phenocrysts size variation (b) and circularity variation (c) are shown with distance from the gouge. Both box plots show 25th and 75th percentile, the median value and whiskers outlining the 1–99% range. Diamonds represent outliers within the dataset and squares are the mean value per sample connected by the dashed line. Errors were calculated from repeat thresholding of the crystals and re-analysis.

165x109mm (300 x 300 DPI)

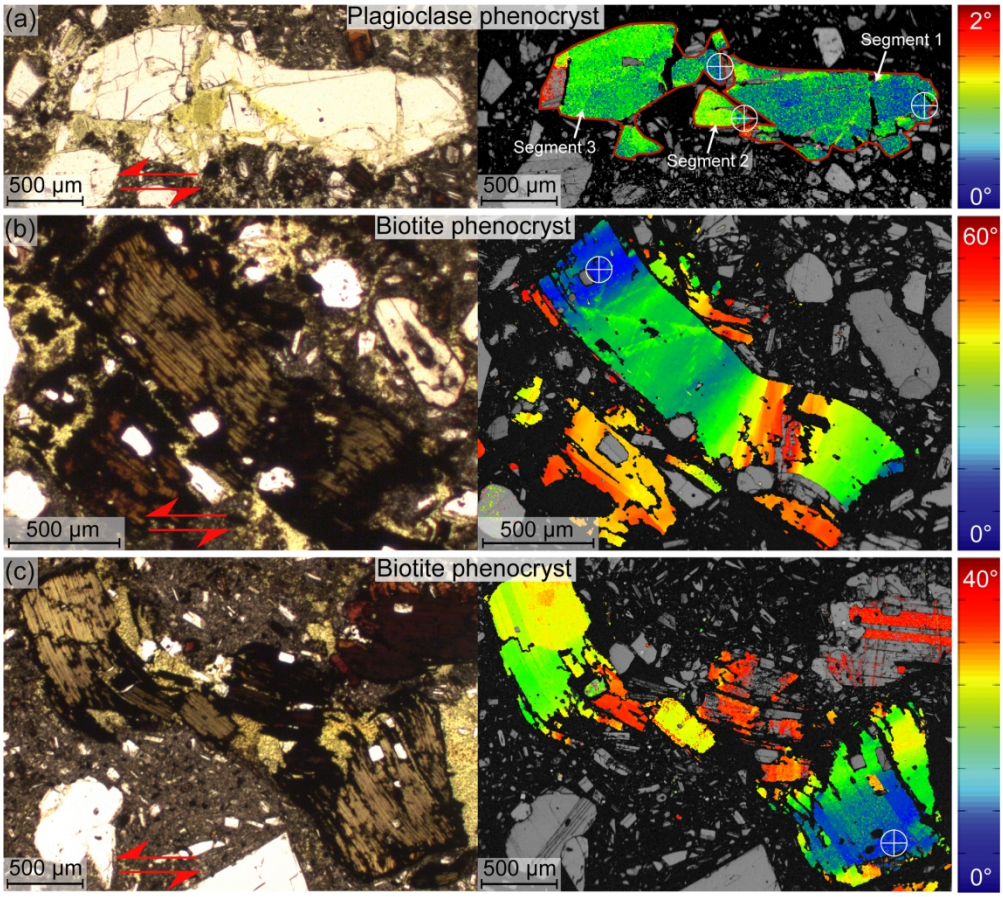

Fig. 8. Plastic deformation of plagioclase and biotite phenocrysts measured by electron backscatter diffraction (EBSD). For each panel (a–c), the left-hand side shows a plane polarised light photomicrograph of the crystal analysed and on the right-hand side is the corresponding band-contrast misorientation map. Colours represent the amount of misorientation relative to a selected point along the crystal, with an angular resolution of ± 0.5º. All points were chosen at one end of the crystal in order to observe the maximum misorientation along the crystal's major axis and are labelled in (a–c) with a white circle and cross. (a) Three fractured segments of a single plagioclase phenocryst from the gouge (Fig. 2b) displaying negligible internal deformation across each. Unlike plagioclase, biotite phenocrysts display extensive plastic deformation throughout the high shear zone. (b) A plastically deformed biotite crystal from the high shear zone (Fig. 2d), revealing a partial tear upon reaching its plastic limit in areas of highest lattice distortion. (c) A biotite phenocryst that deformed plastically in the high shear zone (Fig. 2d), producing an S-C style fabric, and ruptured along a shear band parallel to the extrusion direction, forming fragments with variable plasticity.

164x146mm (300 x 300 DPI)

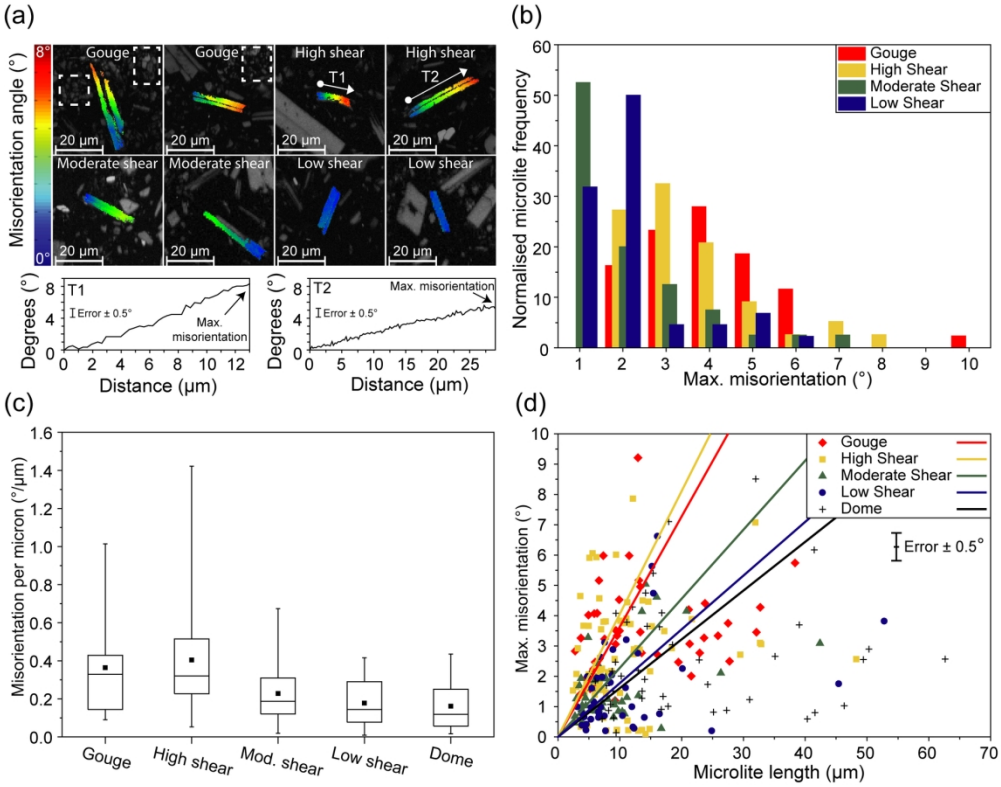

Fig. 9. Plastic deformation of plagioclase microlites across the shear zone. (a) Greyscale band contrast maps with plagioclase microlites subjected to a texture component analysis. The colour gradient displays the relative misorientation across a single microlite grain, thresholding to display up to 8º lattice distortion, and visualised by drawing misorientation transects along the crystals' axis from blue to red (T1 and T2). All misorientation angles have resolution error of ± 0.5º. The dashed outlined areas in the gouge indicate crystalline silica phases owing to glass alteration. (b) Normalised frequency histogram of crystal plastic distortion from each section of the shear zone, binned every 1º misorientation. (c) Box plot of the intensity of plastic deformation represented by the misorientation per micron. The box highlights the 25th and 75th percentiles (the bottom and top of the boxes, respectively) and the whiskers show the data range. The horizontal line in the box marks the median value and the square represents the mean for each section of the shear zone. (d) Maximum misorientation within a single plagioclase microlite versus its length. The gradients of the lines represent the modelled degree of crystal lattice distortion for a given crystal length in each section of the shear zone. These misorientation gradients were modelled by multiplying the mean misorientation per micron, as shown in (c), by an infinite crystal length. Plagioclase microlites in the undeformed dome block were also analysed for comparison.

165x129mm (300 x 300 DPI)

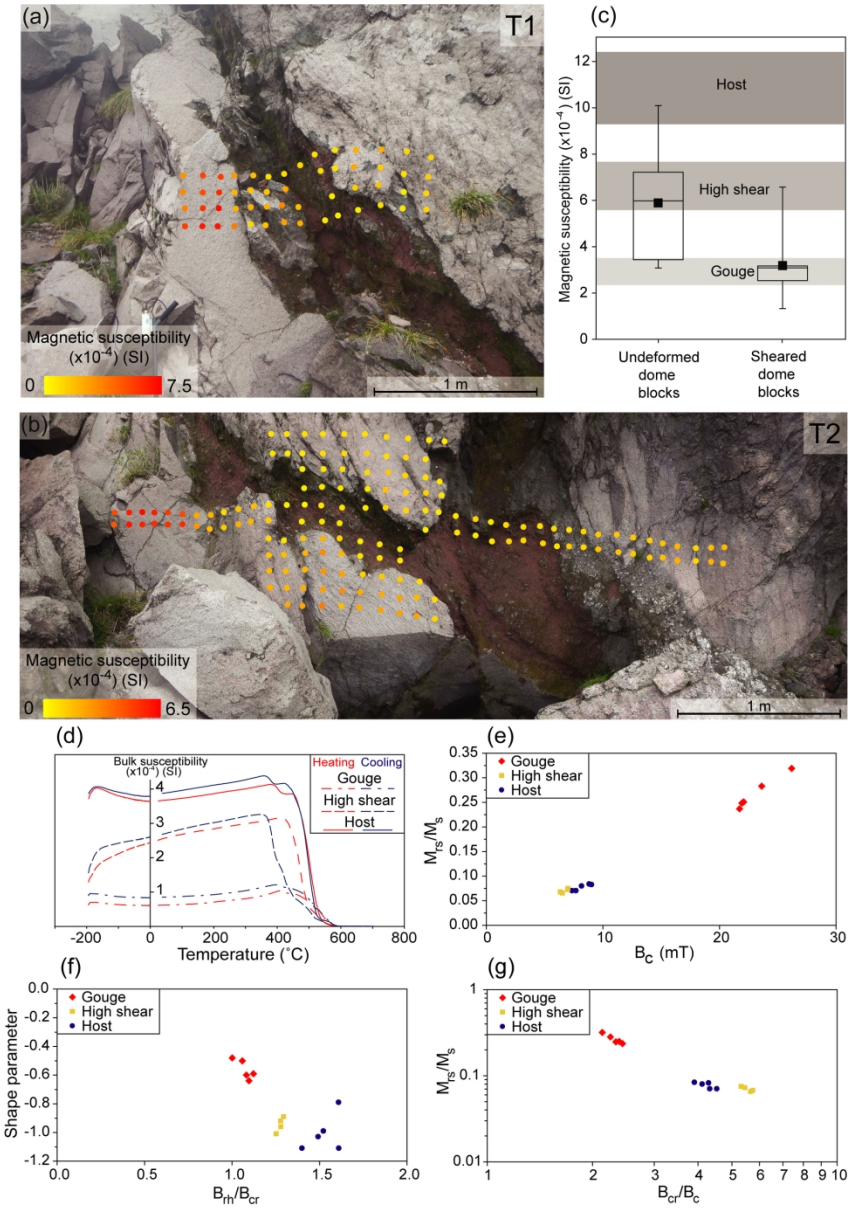

Fig. 10. Field and laboratory magnetic susceptibility measurements. (a, b) Magnetic susceptibility across two different transects of the spine margin at outcrop 2 (T1 and T2 in Fig. 3a), measured using a Bartington portable magnetic susceptibility meter. The undeformed host rock (left in both panels) has the highest susceptibility, gradually decreasing through the highly sheared area to the lowest values in the red gouge layer and finally slightly higher values in the fault breccia on the right of the gouge. (c) Box plot of field magnetic susceptibility measurements of pristine and sheared loose dome rocks, which show values that are comparable to transects in (a) and (b). These are compared to laboratory magnetic susceptibility measurements (marked grey zones; measured using a VFTB) on the host rock, highly sheared coherent lava and gouge. (d) Temperature-dependent bulk susceptibility during heating and cooling cycles (measured using a Kappabridge) for the three rock types. Susceptibility is highest in the host, intermediate in the highly sheared zone and lowest in the gouge and that the magnetomineralogy and stability are distinguishable. (e) Comparison of the ratio of saturation remanence and saturation magnetisation (M_{rs}/M_s) to the coercive force (B_c), showing that the gouge has significantly different remanence carriers. (f) Day plot combining

hysteresis and backfield data showing each section of the shear zone has discrete differences. (g) M_{rs}/M_s against the coercivity ratio (B_{rh}/B_{cr}) reinforces the disparate evolution of the high shear and gouge from the host lava.

160x227mm (300 x 300 DPI)

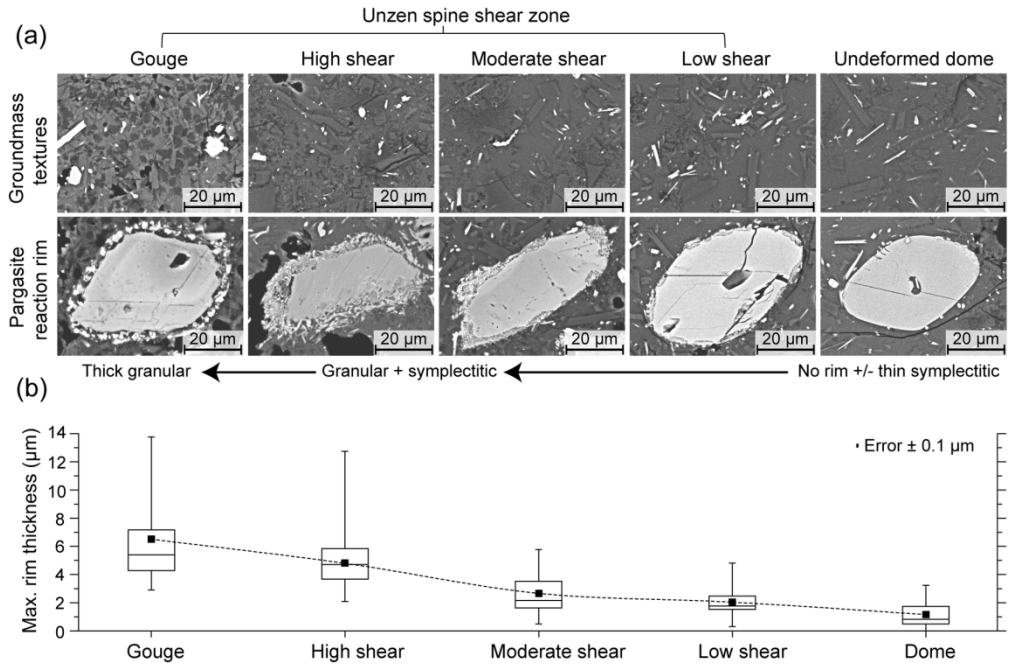

Fig. 11. (a) Backscatter electron (BSE) images of the groundmass textures across the shear zone showing the progressive alteration of the groundmass glass and variations in pargasite reactions rims, both compared to the undeformed dome block. In the low shear zone and undeformed dome block, clusters of small, dark grey silica-rich patches are located around microlites. These clusters in the moderate shear zone spread into web-like domains that increase in abundance in the high shear zone. The gouge is textural distinct from the rest of the shear zone, consisting of larger silica-rich patches that are well distributed within the groundmass. Pargasite crystals are surrounded by granular rims in the gouge material, both granular and symplectitic rims in the high shear zone, and symplectitic rims only in the moderate and low shear zones, with the undeformed dome block showing negligible reaction rims. (b) Box plot showing the maximum thickness of pargasite reaction rims for >30 crystal measured per section of the shear zone. The plot shows the 25th and 75th percentiles, data range, median value (horizontal line) and mean value (square). Thickness error was calculated from the pixel resolution of the BSE images. Pargasite rim thicknesses show an average increase towards the gouge.

163x107mm (300 x 300 DPI)

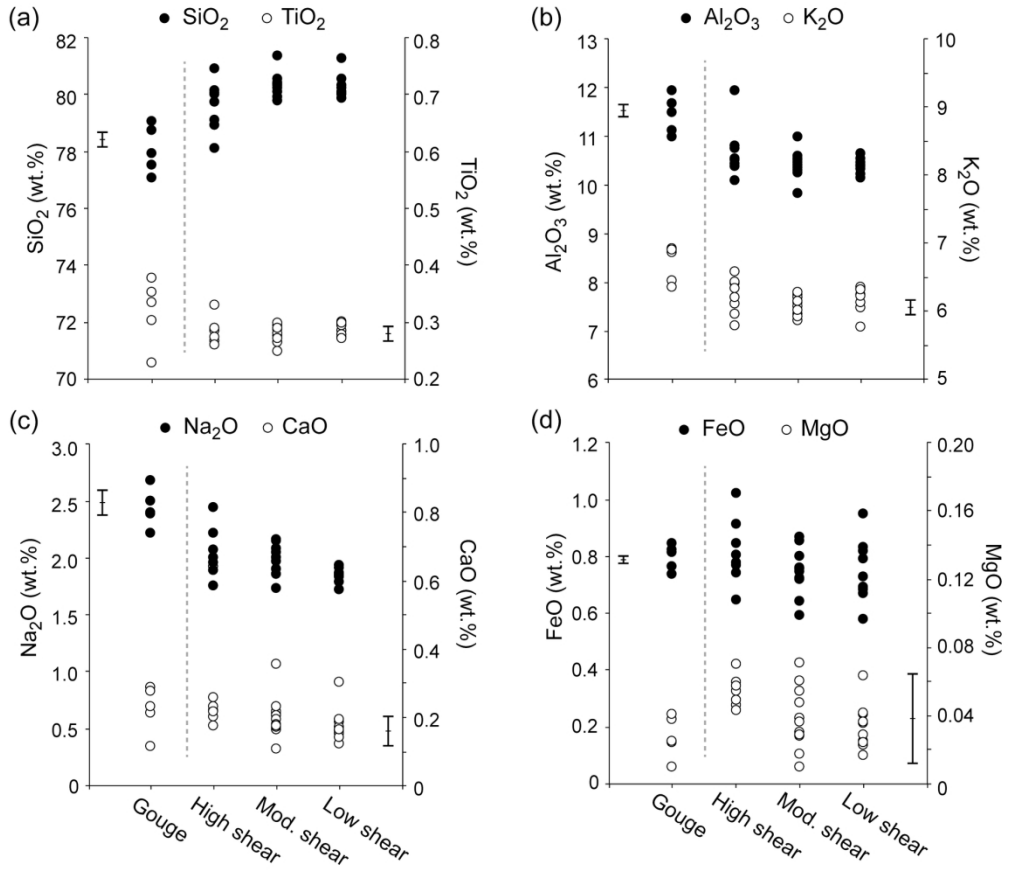

Fig. 12. Composition of the interstitial glass across the shear zone. (a) SiO_2 and TiO_2. (b) Al_2O_3 and K_2O. (c) Na_2O and CaO. (d) FeO and MgO. All values are presented on a volatile-free basis, with totals normalised to 100 wt %. Error bars adjacent to the corresponding component axis denote the relative uncertainty based on repeat analyses of KN-18 glass standard.

166x144mm (300 x 300 DPI)

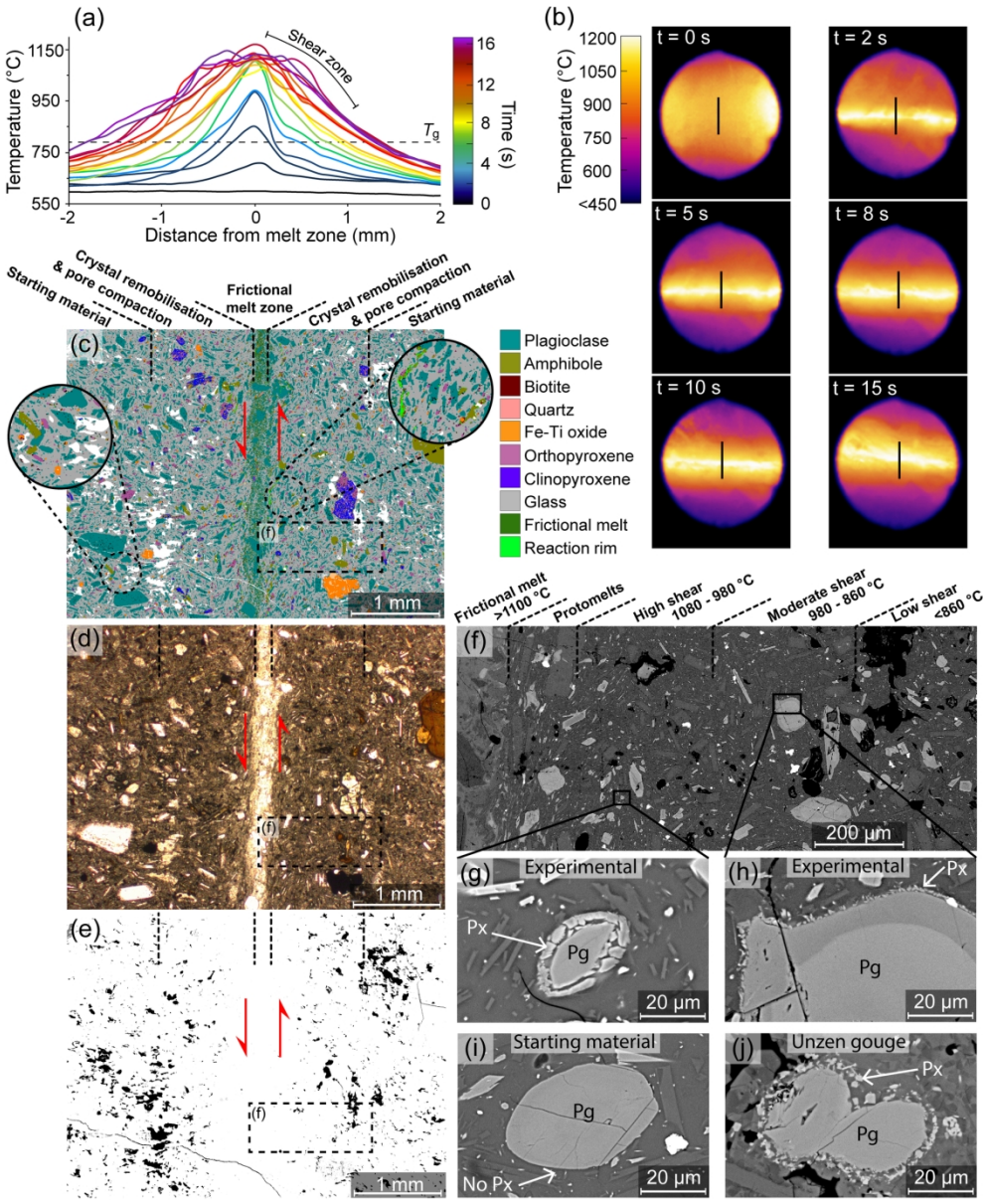

Fig. 13. High-temperature, high-velocity rotary shear (HVR) experiment and associated textures of the experimental shear zone. (a) Temperature evolution across a 2 mm transect of the slip zone through time derived from the thermographic recording of the experimental slip zone (b). The dashed line in (a) denotes the calorimetric glass transition (790 ºC) equating to a viscosity of 10^{12} Pa.s. (b) After ~10 seconds of slip, shear bands are observed radiating from the slip zone. The line across the slip zone in the thermographic images represents the location of the transect used to obtain the temperature profile in (a). Textural observations in (c), (d) and (e) can be directly compared to the temperature profile above. (c) QEMSCAN map and (d) photomicrograph showing the remobilisation of crystals and their alignment adjacent to the melt zone. (e) Porosity distribution showing pores within the shear zone progressively decrease in size and abundance towards the slip plane. (f) BSE image of the experimental shear zone, being dividing into four zones similar to outcrop 1 shear zone, along with temperature estimates for each zone using the temperature profile in (a). Pargasites (Pg) in the experimental shear zone display pyroxene (px) reaction rims in the areas of elevated temperatures, being granular at the highest temperatures (g) and becoming

finer further away (h). (i) Example of a pargasite crystal in the starting material displaying no reaction rim. (j) A pargasite crystal from the gouge displaying a granular rim comparable to (g).

165x201mm (300 x 300 DPI)

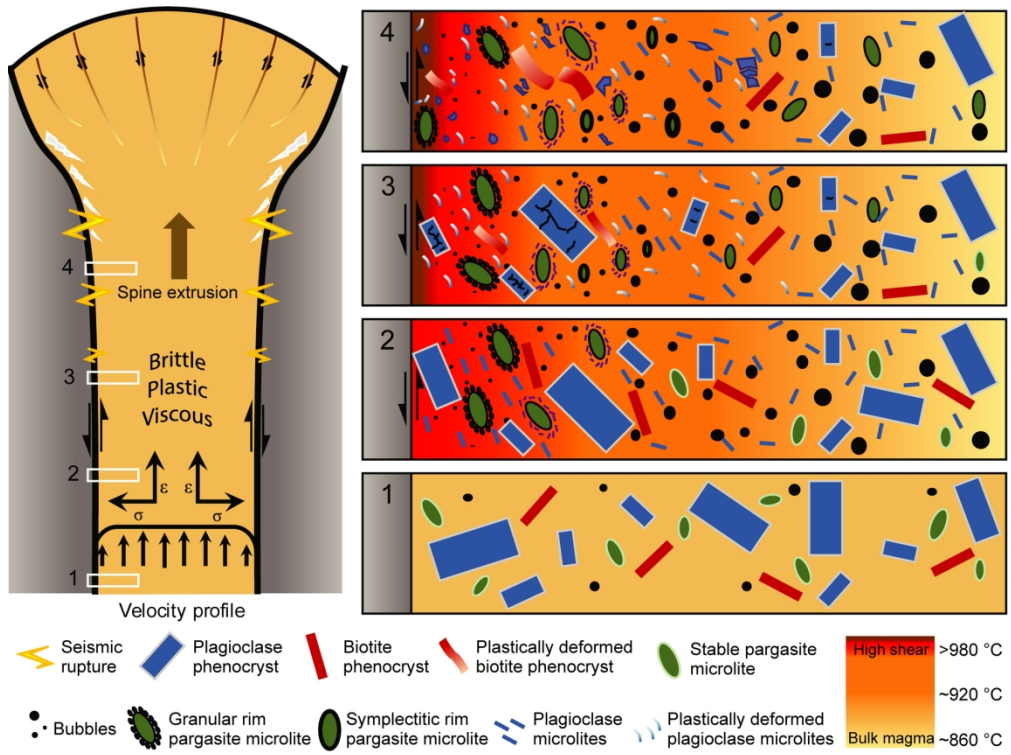

Fig. 14. A conceptual model of the shallow conduit at Unzen volcano prior to the extrusion of the 1994–1995 lava spine. Panels 1–4 represent the textural evolution of plagioclase, pargasite, biotite and pores (bubbles) during magma evolution to the surface. The colour gradient across the transects of the conduit represents a temperature profile derived from the rotary shear experiment. During magma ascent (1), an increase in crystallisation and volatile exsolution causes the flow to transition from a Poiseuille flow regime to a plug style ascent. An increase in viscosity of the crystal-rich magma permits strain to localise near the conduit margins causing deformation and formation of shear zones (2). Here, the increase in stress is manifested in the form of crystal rotation and alignment at the conduit margins. A thermal input likely accompanies viscous deformation due to shear heating, which causes a localised higher-temperature region towards the conduit margins resulting in the destabilisation of pargasite in the form of granular breakdown rims and pore compaction. As magma ascends further (3), it encounters the viscous-brittle transition, where biotite phenocrysts and plagioclase microlites can accommodate strain by deforming plastically with crystal plasticity increasing towards the conduit margin. With further ascent, magma enters the brittle regime (4) causing strain localisation to be expressed by crystal comminution, which increases towards the conduit margins, where stress and strain are highest. The onset of brittle failure is accompanied by characteristic seismicity, as recorded during the extrusion of many domes and lava spines, where frictional behaviour takes over along the conduit margins. The slow extrusion of the high-temperature viscous spine is envisaged to experience late-stage oxidation, resulting in the formation of symplectitic pargasite breakdown rims accompanied with glass devitrification.

165x123mm (300 x 300 DPI)

TABLE 1

Table 1: Whole-rock chemical analyses of major and trace elements from outcrop 1 shear zone

Sample:	A	C	E	H
Rock type:	Lava spine	Lava spine	Lava spine	Lava spine
Zone:	Gouge	High shear	Moderate shear	Low shear
(wt.%)				
SiO_2	65.41	65.88	65.71	65.55
TiO_2	0.70	0.66	0.62	0.62
Al_2O_3	15.49	15.34	15.30	15.58
Fe_2O_3*	5.04	4.87	4.74	4.68
MnO	0.10	0.10	0.10	0.10
MgO	2.45	2.40	2.38	2.29
CaO	4.50	4.51	4.61	4.61
Na_2O	3.57	3.58	3.61	3.65
K_2O	2.52	2.56	2.49	2.47
P_2O_5	0.06	0.10	0.09	0.09
LOI	0.17	0.11	0.18	0.26
Total	100.01	100.11	99.83	99.90
(ppm)				
Ba	498.06	480.96	464.98	477.13
Ce	23.41	51.93	38.11	43.00
Cu	20.75	20.57	28.52	21.55
La	20.93	25.47	21.32	22.20
Nb	13.85	13.53	13.67	13.38
Rb	86.88	84.63	83.50	82.06
Sc	11.43	13.38	12.31	10.99
Sr	289.38	286.58	293.35	304.13
V	80.73	86.91	87.58	91.18
Y	16.47	17.32	18.38	17.12
Zn	48.81	45.59	47.42	45.98
Zr	152.47	144.15	145.65	140.29

Major and trace elements measured by XRF.
* Total Fe as Fe_2O_3.

TABLE 2

Table 2: Bulk mineralogy and groundmass phase abundance of outcrop 1 derived from QEMSCAN

	Sample:	A		C		E	H	
	Rock type:	Lava spine		Lava spine		Lava spine	Lava spine	
	Zone:	Gouge		High shear		Moderate shear	Low shear	
		Bulk	Groundmass	Bulk	Groundmass	Bulk	Bulk	Groundmass
Phases (area % of solid fraction)	**Plagioclase**	37.7	33.1	34.4	28.5	37.2	40.2	27.2
	Amphibole	9.3	4.9	6.6	3.2	6.8	7.7	3.9
	Biotite	3.3	1.2	2.7	0.7	2.5	1.9	0.9
	Si polymorph*	18.4	21.4	14.1	14.8	12.3	12.1	17.0
	Orthopyroxene	1.1	1.3	1.1	1.3	0.9	0.9	1.5
	Clinopyroxene	0.8	0.6	0.7	0.3	0.7	0.8	0.3
	Fe-Ti oxide	0.7	0.4	0.7	0.4	0.7	0.7	0.5
	Apatite	0.1	0.0	0.1	0.1	0.2	0.2	0.2
	Interstitial glass$	24.6	33.5	36.3	47.7	35.2	32.0	45.6
	Boundary phases#	4.0	3.6	3.3	3.0	3.5	3.5	2.9
	Total	100.0	100.0	100.0	100.0	100.0	100.0	100.0
	Porosity (area %)	16.1	19.2	13.2	13.0	19.0	22.4	18.7

All mineral phases and glass abundances are normalised on a pore-free basis.
* combines all SiO_2 polymorphs (including quartz and cristobalite).
$ includes any partially devitrified glass and associated groundmass SiO_2 phases smaller than the beams interaction volume (~10 μm^3).
# denotes when the beam interacts at the boundary between 2 or more phases.

TABLE 3

Table 3: Laboratory-based magnetic properties of outcrop 2 shear zone: Magnetic susceptibility, Curie temperature, degree of saturation and coercivity of remanence

Magnetics measurement:	Sample no.:	Host	High shear	Gouge
Magnetic susceptibility (10^{-4} SI units)	1	9.70	6.11	1.85
	2	8.97	5.21	2.25
	3	12.10	7.22	2.46
	4	10.70	6.39	3.10
	5	9.24	–	2.98
	Average	10.14	6.23	2.53
Curie Temperature, T_C (°C)	1	522	509	552
	2	509	507	559
	3	533	506	555
	4	520	–	521
	5	–	–	533
	Average	521	507	544
Degree of saturation, S300 (at 300 mT)	1	0.99	0.95	0.91
	2	0.99	0.95	0.91
	3	1.01	0.98	0.91
	4	1.00	0.96	0.93
	5	0.98	–	0.94
	Average	0.99	0.96	0.92
Coercivity of remanence, B_{cr} (mT)	1	33.39	36.43	55.86
	2	33.66	37.29	53.17
	3	33.28	36.95	52.59
	4	38.81	38.06	51.10
	5	34.55	–	52.88
	Average	34.74	37.18	53.12

TABLE 4

Table 4: Composition of the interstitial glass from outcrop 1 shear zone

Sample:	**A**	**C**	**E**	**H**
Rock type:	Lava spine	Lava spine	Lava spine	Lava spine
Zone:	Gouge	High shear	Moderate shear	Low shear
n	5	8	13	10
SiO_2	78.08 (0.75)	79.64 (0.82)	80.26 (0.42)	80.32 (0.38)
TiO_2	0.32 (0.05)	0.29 (0.02)	0.28 (0.01)	0.29 (0.01)
Al_2O_3	11.42 (0.35)	10.67 (0.51)	10.42 (0.26)	10.40 (0.14)
FeO*	0.80 (0.04)	0.81 (0.11)	0.73 (0.09)	0.74 (0.10)
MgO	0.04 (0.01)	0.06 (0.02)	0.04 (0.02)	0.04 (0.01)
CaO	0.22 (0.06)	0.27 (0.14)	0.20 (0.06)	0.18 (0.05)
Na_2O	2.43 (0.15)	2.04 (0.20)	2.00 (0.13)	1.85 (0.06)
K_2O	6.69 (0.24)	6.22 (0.25)	6.07 (0.12)	6.18 (0.17)
Total	100.00	100.00	100.00	100.00
Σ	99.89	99.79	100.61	99.82

Normalised average compositions of the interstitial glass across the outcrop 1 shear zone. Numbers in parentheses show the standard deviation (1σ) derived from multiple analyses.
n, number of microprobe analyses averaged to determine the average glass composition and standard deviation.
* Total Fe as FeO.
Σ, averaged original microprobe totals.